



RPSEA

Phase 1 Final Report

09121-3300-06.Phase1FINAL

High Resolution 3D Laser Imaging for Inspection, Maintenance, Repair, and Operations

Contract: 09121-3300-06

March 9, 2012

Carl Embry
Chief Technologist / Partner
3D at Depth, LLC
5733 Central Avenue
Boulder, CO 80301

LEGAL NOTICE

This report was prepared by 3D at Depth, LLC as an account of work sponsored by the Research Partnership to Secure Energy for America, RPSEA. Neither RPSEA members of RPSEA, the National Energy Technology Laboratory, the U.S. Department of Energy, nor any person acting on behalf of any of the entities:

- a. **MAKES ANY WARRANTY OR REPRESENTATION, EXPRESS OR IMPLIED WITH RESPECT TO ACCURACY, COMPLETENESS, OR USEFULNESS OF THE INFORMATION CONTAINED IN THIS DOCUMENT, OR THAT THE USE OF ANY INFORMATION, APPARATUS, METHOD, OR PROCESS DISCLOSED IN THIS DOCUMENT MAY NOT INFRINGE PRIVATELY OWNED RIGHTS, OR**
- b. **ASSUMES ANY LIABILITY WITH RESPECT TO THE USE OF, OR FOR ANY AND ALL DAMAGES RESULTING FROM THE USE OF, ANY INFORMATION, APPARATUS, METHOD, OR PROCESS DISCLOSED IN THIS DOCUMENT.**

THIS IS AN INTERIM REPORT. THEREFORE, ANY DATA, CALCULATIONS, OR CONCLUSIONS REPORTED HEREIN SHOULD BE TREATED AS PRELIMINARY.

REFERENCE TO TRADE NAMES OR SPECIFIC COMMERCIAL PRODUCTS, COMMODITIES, OR SERVICES IN THIS REPORT DOES NOT REPRESENT OR CONSTITUTE AN ENDORSEMENT, RECOMMENDATION, OR FAVORING BY RPSEA OR ITS CONTRACTORS OF THE SPECIFIC COMMERCIAL PRODUCT, COMMODITY, OR SERVICE.

Abstract

In January 2011, 3D at Depth was awarded a RPSEA contract to bring high-resolution three-dimensional (3D) laser imaging technology from the lab into an underwater environment for the oil and gas industry. During the project, CDL Inc. provided expert engineering support and materials to marinize the system. The project included two underwater trials which demonstrated the feasibility of utilizing high resolution laser detection and ranging (LADAR) in a subsea environment.

3D laser imaging is a powerful data collection system that provides 3-D information for a specific area of interest. It is the predominate technology for terrestrial survey, construction, as-built analysis, and large-scale retro-fits. The 3D laser imaging market is a mature multi-billion dollar industry with an eco-system of software, expertise, and best practices. Developing the technology to provide high-definition subsea laser imaging enables the deep water industry to use the current state of the art in 3D metrology and related best practices developed for the terrestrial market.

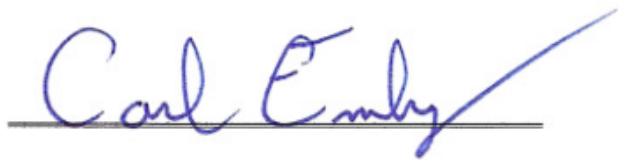
Terrestrial laser scanners commonly produce centimeter spatial and range accuracy at several hundred meter range. Due to the absorption of water, realizable deep-water systems are limited to tens of meters range depending on the target and water conditions. To our knowledge, this RPSEA program enabled a world's first demonstration of 3mm measurement accuracy at greater than 8 meter range for an underwater laser sensor integrated with a ROV.

This final report documents the development of the underwater laser scanning system over the last year by 3D at Depth and CDL under the RPSEA program. The first section discusses some of the theoretical background of underwater laser sensing and shows results from 3D at Depth's simulators. Following are descriptions of the prototype sensor, experimental configuration for the underwater pool tests performed in September 2011, and results from those tests. The ROV test experimental configuration is then discussed along with results from those tests performed at Schilling Robotics in Davis, CA in February 2012. This section is followed by results of the preliminary reliability tests including the transit case tests. These results are summarized and directions for Phase 2 work are presented in the final section.

This technology is essential for better management of deep water assets. The lack of timely and accurate survey-quality 3D measurements poses an integrity management challenge for such assets. A lack of accurate data results in either higher risks or higher costs to build and maintain environmentally safe production and product transportation systems. The speed and precision of the technology developed by this project reduces operating costs for underwater inspection, maintenance, and repair; reduces environmental risk through more accurate inspection; and significantly improves construction quality/reliability through rapid access to sharable survey-quality as-built data before, during and after construction.

The Phase 1 goals for this technology development program were all met and are still in-line with industry requirements. With the successes demonstrated in Phase 1, we envision that by the end of Phase 2 the technology will be ready for demonstrations in ultra-deep water field operations to enable better integrity management of assets by providing real-time survey quality 3D data.

Signature and Date Stamp



Carl Embry
Chief Technologist / Partner

March 9, 2012

Date

THIS PAGE INTENTIONALLY LEFT BLANK

Table of Contents

1	Introduction.....	6
2	Theoretical Background and Simulations.....	7
3	The Sensor	11
4	Pool Technology Trial	12
4.1	Experimental Configuration.....	13
4.2	Underwater Test Results and Discussion.....	14
5	ROV Technology Trial	21
5.1	Custom Power Supply.....	21
5.2	ROV Experimental Configuration	22
5.3	ROV Underwater Test Results and Discussion.....	25
6	Reliability Testing.....	31
6.1	Thermal Testing	32
6.1.1	Operating Temperature	33
6.1.2	Thermal Cycling (Storage Temperature).....	33
6.2	Shock and Vibration Testing.....	34
6.2.1	Vibration Testing	34
6.2.2	Shock Testing.....	35
6.3	Final Inspection.....	36
6.4	Transit Case Testing.....	36
7	Conclusions.....	39
8	References.....	43

List of Figures

Figure 1. Jerlov curves showing transmittance percentage per meter traveled vs. wavelength. .. 8

Figure 2. Theoretical range performance for one version of the prototype system..... 10

Figure 3. Output of laser scanner simulator. CAD model and simulated sensor (Left). Simulated point cloud data (Right). 11

Figure 4. Block diagram of 3D laser scanning sensor. 11

Figure 5. Prototype sensor mounted on a tripod with standard subsea camera mounted on top (Left). Programmable +/- 15° scan area in both azimuth and elevation provides 4.3m swath at 8m range (Right). 12

Figure 6. 3D laser sensor on tripod connected to lab power supply on rolling cart (Left) 3D laser sensor and tripod in pool with subsea cables connecting to the lab power supply outside the pool (Right). 13

Figure 7. Topside control with a standard laptop through a standard Ethernet connection (Left) . Laser sensor illuminating targets on the opposite side of the pool (Right). 13

Figure 8. Tripod target used for range verification testing. 14

Figure 9. Multiple objects scanned at once. Image from HDTV underwater camera while performing a large area scan (Left). Resulting 3D data where color is mapped to range – blue is short range (Right). 15

Figure 10. Rusted, angled flange target (Left). The attitude is not identifiable with a straight-on orientation (Right). 16

Figure 11. 3D Data of rusted flange. Isometric view shows the flange and shadow on the back wall (Left). Rotating the data 90° allows identification and measurement of features such as the flange attitude (Right). 16

Figure 12. 10 inch diameter yellow flange (Left). Standard metal chain attached during the scan (Right). 17

Figure 13. 3D data of yellow flange Lower resolution scan does not show chain detail (Left). Higher resolution scan does show chain detail (Right). 17

Figure 14. Scan of 8 inch diameter pipe (Left). Blue crate to simulate protective gratings (Middle). Scan with blue crate behind pipe (Right). 18

Figure 15. 3D data of 8 inch pipe at 5.9m range. Isometric view shows the pipe, crate, and pool wall all in one scan (Left). Same data rotated 90° reveals the 3mm and < 1mm holes in the pipe (Right). 18

Figure 16. 3D point cloud data can be processed in standard software 3D model is generated in Leica Cylcone and a section cut is made at the dent (Top). The model and section cut are output into .dxf format and then imported into AutoCAD to make measurements of the pipe and dent (Bottom). 19

Figure 17. 3D data of Firestone Firehawk Tire at 6.1 meter range..... 20

Figure 18. Tests on different survey targets. Photo of survey targets on docking platform (Left). 3D point cloud of survey targets (Middle). Solid model of survey targets (Right). 20

Figure 19. Custom power board sitting on top of the lab power supplies. The custom design enables integration of the power supply inside the underwater housing. 22

Figure 20. Laser sensor integrated with Schilling UHD ROV. 22

Figure 21. A single subsea cable provides both power and communications to the laser sensor.23

Figure 22. Power and communications are delivered to the ROV through a 450 meter tether. .. 23

Figure 23. ROV control center. Displays show two ROV mounted cameras, one tank mounted camera, one crane mounted camera, and the laser sensor control screen which is displaying data in the top right screen..... 24

Figure 24. A Hot stab panel was used as the primary target for this test..... 24

Figure 25. The ROV is lowered into the test pool with a crane (Left). The ROV is completely submerged and ready for test (Right)..... 25

Figure 26. The distance between bolts was measured on land with a tape measure prior to lowering the hot stab panel into the pool. 25

Figure 27. The laser spot is easily seen on the standard ROV camera monitor. 26

Figure 28. Hot stab panel as viewed from main ROV camera monitor (Left). Processed 3D data from laser scanner with color mapped to range – red is furthest distance (Right). 27

Figure 29. Profile view of hot stab panel using the same data from Figure 28. 27

Figure 30. Two fins on the hot stab panel as seen in air (Left) and by the ROV main camera (Right). 28

Figure 31. A single 3D scan of the fins easily shows the depth of the fins along with the writing below..... 28

Figure 32. Still-screen capture of the laser sensor from the ROV main camera showing some of the particulates in the water. Every white spot and streak is a particle. 29

Figure 33. Post processing of 3D data using Leica Cyclone. 30

Figure 34. Hot stab panel data in Cyclone with the supports converted into model cylinders and the spheres converted into model spheres..... 30

Figure 35. Data was collected and processed while ROV was static (Left) and while the ROV was in station keeping mode (Right). 31

Figure 36. Window in thermal chamber allows functional testing of the sensor during thermal tests. 32

Figure 37. Sensor mounted on vibration table for shock and vibration testing. 34

Figure 38. Example accelerometer output during vibration testing for the Z-axis. Accelerometer is in-plane with the Z-axis and matches the input accelerations without resonance (Left). Accelerometer is out-of-plane with the Z-axis and shows no signs of resonance (Right). 35

Figure 39. Example accelerometer output during shock testing for the Z-axis. Shock pulse is

within the accepted tolerances (Top). Outputs from seven accelerometers show no resonance features (Bottom). 36

Figure 40. Housing in transit case with three accelerometers attached (one in each axis)..... 37

Figure 41. Transit case and housing instrumented and ready for 24 inch drop test. 38

Figure 42. Example accelerometer output during drop tests. This data shows a successful packaging test where proper packaging reduced the shock from 300g to 16g. 38

Figure 43. Example accelerometer output during drop tests. This data shows 1000g shock when dropped on the small end of the transit case. 39

List of Tables

Table 1. Range Verification Data	14
Table 2. Measurement Verification Data.....	26

1 Introduction

A critical area for effective construction and asset management operations is quality. Quality in manufacturing leads to more consistency, less down time and lower repair costs. This is significant when the assets are generating millions of dollars per day. One of the cornerstones of quality in construction and asset management is measurement and survey. Accurate surveying leads to more precise construction, and more accurate inspection reduces costly down time by finding issues before they arise. A lack of accurate data results in higher risks or costs to build and maintain environmentally safe production and product transportation systems. Better measurements equates to better management.

Subsea construction, inspection and maintenance processes and their associated technologies have not kept pace with their land based counterparts. On land, the survey and measurement industry was transformed by the introduction of 3D laser scanning technologies. The laser scanning market is a mature, multi-billion dollar industry with an eco-system of hardware, software, expertise and best practices. 3D laser scanners quickly produce precise, high resolution 3D models of as-built facilities and are used throughout the construction and maintenance process.

Conversely, the technologies for undersea surveying and measurement are relatively coarse and include two main technologies: video and SONAR. Video provides a method for visually inspecting assets but does not provide quantitative information – only 2D information. Attempts have been made to acquire 3D data underwater with camera using methods such as photogrammetry and stereo imaging.^{1,2,3} Major limitation with these approaches are reconstructions in areas of low textural information, poor image contrast due to water conditions, and shadowing due to directional lighting.⁴

SONAR systems have been the main tools for measurement and survey for many years and have become very sophisticated. Many companies have developed high resolution multi-beam sonar systems which can produce angular resolutions as small as 0.2° . However the resolution of these systems are fundamentally limited due to the underlying physics – the wavelength of light is over 10^8 times smaller than ultrasonic wavelengths and can achieve angular resolutions of less than $100\mu\text{rad}$ (0.006°). Therefore light based sensors inherently have higher spatial resolutions than sonar systems.

Multiple underwater systems have been developed in the past to take advantage of the high resolutions achievable with lasers. A literature search reveals that both triangulation and range gated (or Time of Flight) underwater systems have been investigated over the last several decades.

Laboratory versions of triangulation based laser imagers in clear water and short range (0.2 – 0.4m) were developed and demonstrated since the mid-1990s.^{5,6,7,8} Even at that time, triangulation systems were noted for providing high resolution at close range (less than 3m), while range-gated systems could provide better resolution at longer ranges.

A triangulation based system was developed by K. Moore at the Scripps Institute of Oceanography in 2000 for bathymetry.⁹ This system was designed to provide approximately 3 mm accuracy depth information at 2m range that degraded exponentially with range. Depth resolution errors would approach 10 centimeters at 10 meter range.

More recently, another triangulation system was developed for seafloor roughness

measurements. This system operated approximately 75centimeters above the seabed and produced approximately 0.3mm(x) x 0.5mm(y) x 0.3mm (depth) resolutions while deployed off the New Jersey coast.¹⁰ Note that the range is generally less than 3m for these triangulation systems. This is a fundamental limitation of the triangulation method for calculating range, and thus limits its usefulness as a general underwater survey tool.

Many of the terrestrial laser imagers available on the market today are based on Time of Flight (ToF) technology. This includes products such as the Leica ScanStation C10, the Trimble CX Scanner, and the Optech ILRIS-3D. These ToF sensors use a laser to emit a pulse of light. An accurate timer is used to time how long it takes for the pulse of light to travel to and from a target. This time is then used to calculate the range to the target based upon the speed of light. There is no fundamental limitation on the range of a ToF sensor besides the ability to detect the return photons reflected off the target (ToF ladars are used to measure the distance to satellites). Therefore highly reflective objects can be detected at longer ranges than low reflectivity targets.

A literature search will reveal that scanning, pulsed, 3D laser imagers have been investigated and deployed underwater over the last couple of decades for military purposes^{11,12,13,14}. Some of these are underwater based and others are aircraft based to detect underwater mines. In either case, these systems did not attempt to achieve the range and spatial accuracies provided by current terrestrial laser scanners (sub-inch).

The underwater 3D laser sensor developed under this RPSEA contract has the fundamental advantage of providing sub-centimeter precision at greater than 8m range, a capability that to the authors' knowledge has not been previously demonstrated.

This final report documents the development of the underwater laser scanning system over the last year by 3D at Depth and CDL under the RPSEA program. The first section discusses some of the theoretical background of ToF underwater laser sensing and shows results from 3D at Depth's simulators. Following are descriptions of the prototype sensor, experimental configuration for the underwater pool tests performed in September 2011, and results from those tests. The ROV test experimental configuration is then discussed along with results from those tests performed at Schilling Robotics in Davis, CA in February 2012. This section is followed by results of the preliminary reliability tests including transit case tests. These results are summarized and directions for Phase 2 work are presented in the final section.

2 Theoretical Background and Simulations

In optical detection sensors, light (laser energy) is transmitted through a scattering medium to a hard target. If the target is a rough surface (not a mirror), the energy is scattered into a full hemisphere. Some of this back-reflected energy is captured by the receiver aperture and converted to an electrical signal. The received energy must have enough power to create more signal electrons than the noise level of the receiver to obtain detection.

A single equation predicts the amount of optical signal power collected by the receiver aperture from the target (P_s). This is sometimes called the ladar (laser radar) equation. This equation is common for both direct and coherent detection systems.

$$P_s = P_t \eta_t \eta_r T^2 \rho_\pi \left(\frac{A_r}{R^2} \right) \quad (1)$$

The peak power transmitted by the laser (P_t) is first attenuated by the optics of the remote sensor (η_t). This energy is then attenuated by the extinction (T) of the medium of propagation (sea water). The wavelength of the laser must be chosen carefully to maximize transmittance through the medium. The Jerlov curves can be used to select an appropriate wavelength for seawater.

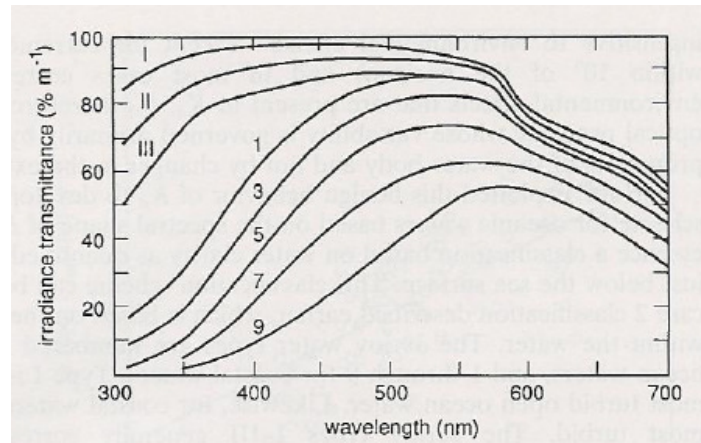


Figure 1. Jerlov curves showing transmittance percentage per meter traveled vs. wavelength.¹⁵

Jerlov defined water types as: I = extremely clear oceanic water; II = tropical/subtropical oceanic water; III = oceanic water at temperate latitude. Curves 1-9 are coastal waters with varying degrees of turbidity. Blue light (approximately 475nm) has the highest transmittance in clear water, but even with mild turbidity the transmittance drops to 85 – 80 percent per meter traveled. Green light (approximately 525nm) has only slightly higher loss in clear water, but has much better performance in highly turbid water (15 - 20 percent per meter higher transmittance). For this reason, along with the fact that 532nm lasers are common, 3D at Depth has chosen green as its laser source.

Back to the lidar equation, a portion of the remaining energy is then back-reflected towards the receive aperture by scattering points on the hard target (structure of interest). The target reflectivity ρ_π (sr^{-1}) defines the power reflectivity of the hard target on a steradian basis. The reflected energy is again attenuated by the extinction (T) of the medium. The reflected power is finally captured by the viewing angle of the receiver, which is again defined in steradians (A_r/R^2), where A_r is the area of the receive aperture, and R is the range to the target. The received power also experiences an optical loss (η_r) due to the laser remote sensor optical components.

Another key parameter for SNR is the target surface reflectivity (ρ_π). Most rough surfaces are well described by a Lambertian surface, where the power of the back-reflected light decreases with angle from normal incidence (θ) by $\cos\theta$. Due to this $\cos\theta$ dependence, Lambertian sources reflect into π steradians for a hemisphere, as opposed to the normal 2π steradians in a hemisphere. Therefore ρ_π for a Lambertian surface is defined as the power reflectivity (a number between 0 and 1) divided by π steradians.

A common conservative value for ρ_π used in lidar modeling is $0.1/\pi$, (or approximately 3.2 percent). For our models we use an even more conservative ρ_π of $0.0354/\pi$ (or 1.1 percent). This is the value of black paint at 532nm published by the NASA Jet Propulsion Laboratory ASTER Spectral Library.¹⁶

In direct detection sensors, the return photons are measured directly with a photo-detector

(usually a semiconductor diode that converts photons to electrons). The fundamental measure of system performance is the signal-to-noise ratio (SNR) which is a measure of the number of signal electrons versus the electron noise floor of the sensor, which includes multiple noise sources. These noise sources include shot-noise from the signal, background light, detector dark current, laser and background light scattering off of particles, and electronics amplifier noise. The fundamental SNR equation is:

$$SNR = \frac{\langle i_s \rangle^2}{\text{var}[i_n]} \quad (2)$$

where i_s is the received signal current and $\text{var}[i_n]$ is the variance of the total current noise. For a direct detection optical sensor in a scattering medium:

$$SNR = \frac{\langle P_s \mathfrak{R} G \rangle^2}{2qB[P_s \mathfrak{R} + P_{Scat} \mathfrak{R} + P_{bgTar} \mathfrak{R} + P_{bgScat} \mathfrak{R} + i_d]F_d G^2 + N_a B} \quad (3)$$

where P_s is the optical power from the target received by the sensor (equation 1), \mathfrak{R} is the responsivity of the detector (which includes the quantum efficiency), and G is the gain of the photo-detector. The units of this quantity is amps^2 of the desired optical signal (the numerator). This quantity must be higher than the noise term, which is the denominator of equation 3. For the denominator, q = the charge value of an electron, B = the bandwidth of the receiver, P_{Scat} is the received energy from the laser pulse scattering off of particles in the water, P_{bgTar} is the background light optical power received that is reflected from the target, P_{bgScat} is the background light optical power received from scattering off of particles in the water, i_d is the photodetector dark current, F_d is the noise factor contributed by the photodetector gain, and N_a is the electronics noise variance. This entire term is the current noise variance and also has units of amp^2 . SNR is an average (not instantaneous) measure of the receiver capability. This is a powerful equation which allows many system tradeoffs.

3D at Depth has a physics-based model in MATLAB to model these noise sources and the SNR to perform trades of the design. Figure 2 below shows the signal and noise sources for one configuration of the prototype sensor assuming Jerlov Type II oceanic water with Turbidity=1 on a black paint target. For this particular simulation the background light was generated by modeling an on-axis ROV headlamp – a Kongsberg OE11-150.

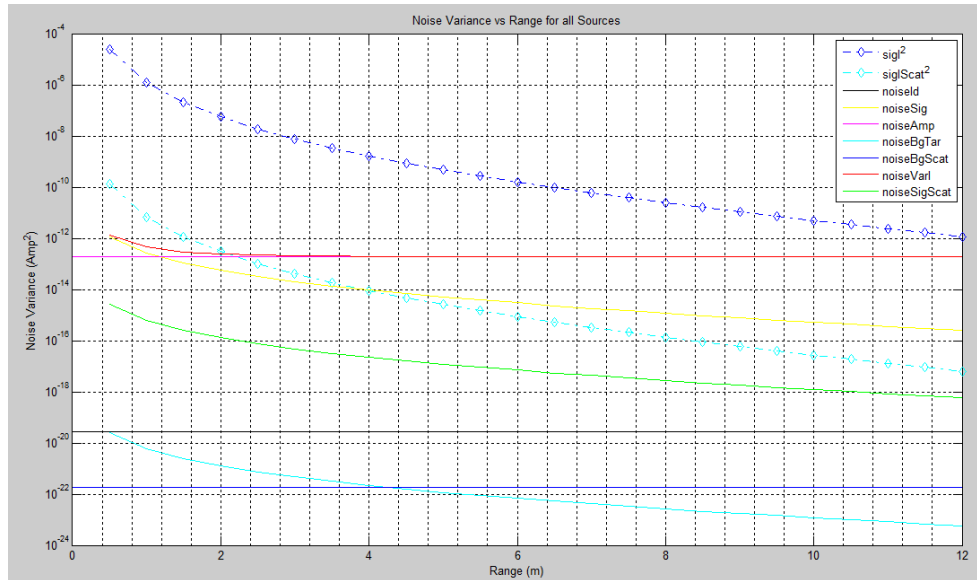


Figure 2. Theoretical range performance for one version of the prototype system.

This performance model clearly shows that the limiting noise factor is the electronics noise (noiseAmp) which prevents the sensor from operating at the shot noise limit. However, the sensor still has SNR of approximately 20dB at 9m range, which allows for good signal detection. 3D at Depth is implementing more sensitive receivers in the next RPSEA phase which will allow the system to operate at the shot noise limit, however we have proven that this is not necessary for greater than 8m operation in clear water conditions.

In addition to the basic range capability of the sensor, another software based simulator was built to model the combined laser range computation and scanning field of view. This simulator is used to study and understand the resultant images possible by scanning at different rates with different scan envelopes.

A 3D CAD model is first generated consisting of a typical pipeline geometry and sea bed, as shown in Figure 3. The simulated laser sensor is positioned above the target geometry per a configurable offset distance and view angle. As the simulation progresses, the laser pulse is directed in a 2 dimensional scan pattern at a simulated scan rate. Each directional laser pulse is searched against the target geometry for intersection and a possible resultant range calculation. This produces a resulting simulated 3D point cloud. The collection of 3D intersections are stitched together to form a 3D image depicting the capability of the sensor for the given target model and scanning parameters. In addition, the simulator has the capability to include a second laser at an angle offset to study how a second laser system provides greater visibility into the target geometry.

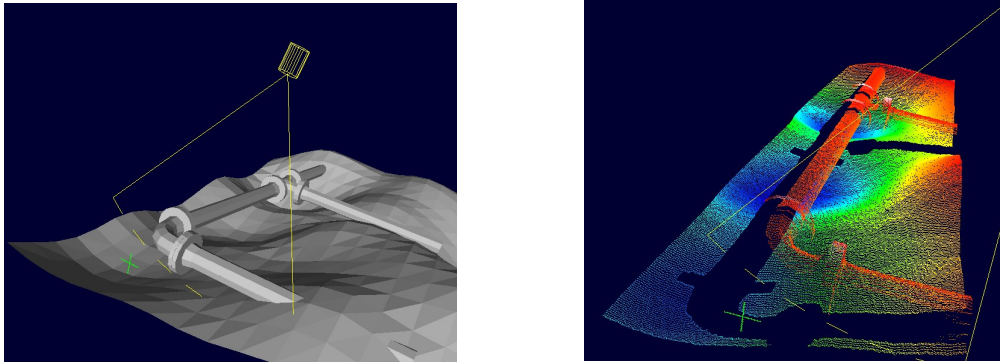


Figure 3. Output of laser scanner simulator. CAD model and simulated sensor (Left). Simulated point cloud data (Right).

This simulator can additionally be used to aid in project management. The simulator can determine initial ROV speed and offset from the target for different mission objectives (size of feature to be detected) prior to deployment. Based on target geometry, the simulator would also provide insight into single or multiple laser system usage to investigate intricate target geometries.

3 The Sensor

The above simulators were used to perform multiple paper designs of the sensor based upon customer requirements, water conditions, various sub-system components, and system configurations. This allowed for the sound technical approach of predicting sensor performance to make trades between different sensor architectures and components prior to building the first unit.

A block diagram of the sensor is shown in Figure 4 below. The optical head (Laser Imaging Unit) consists of the transmitter sub-system (laser and accompanying optics), the receiver subsystem (detector and accompanying optics) and the scanner. These sub-systems can be optimized for different operational scenarios and environmental conditions. For this prototype system we used a diode pumped, passively Q-switched, Nd:YAG laser with an external non-linear crystal to perform the frequency doubling to 532nm laser light. The receiver is a high-speed silicon photodiode, and the scanning subsystem is a two-axis galvanometer scanner to allow programmable scanning in two orthogonal directions.

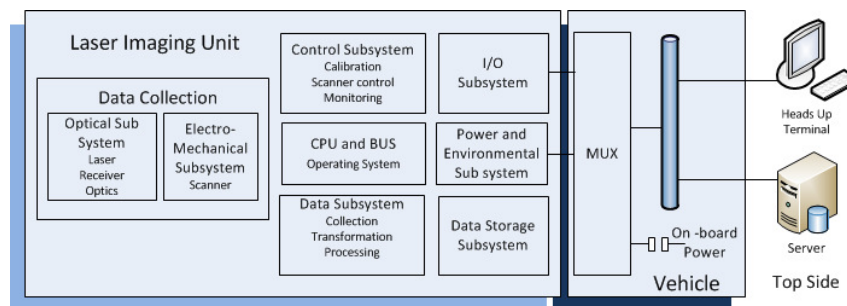


Figure 4. Block diagram of 3D laser scanning sensor.

Along with the Laser Imaging Unit (LIU) are multiple electronic control systems. These include the Control Subsystem for controlling the LIU and monitoring system health; the CPU and BUS for general system control and operation; the Data Subsystem for data collection, transformation and processing; the Data Storage System for housing data locally; the Power and Environmentally Monitoring System to convert the host vehicle power to the various voltages required by the sensor; and the I/O (Communication) subsystem. All of these systems are housed within the subsea sensor.

An Ethernet (TCP/IP) connection is the only communications connection to the outside world. Power is also supplied through standard Burton 5500 Series subsea connectors. In an operational scenario both power and communications are connected directly to the ROV communication and power system (26V DC). Control of the sensor and additional data storage is then performed on the topside boat with a standard laptop or desktop computer. Data processing and visualization can be performed in real time at this topside terminal.

Figure 5 below shows the assembled prototype sensor. The prototype sensor is 8.2 inch diameter, 28 inches long, and weighs 76.1 pounds in air. The aluminum housing and Burton connectors are all designed for 3000m operation. A 2.5-inch diameter window is located on one side of the sensor and is currently designed for 300m operation. A 3000m window will be designed into the system during the next phase of the RPSEA program. The sensor is designed to allow $\pm 15^\circ$ scanning in both azimuth and elevation. This scan area (along with scan rate) is completely programmable by the user at the topside terminal. With an 8 meter range of operation this allows for a maximum 4.3 meter swath per linear scan.

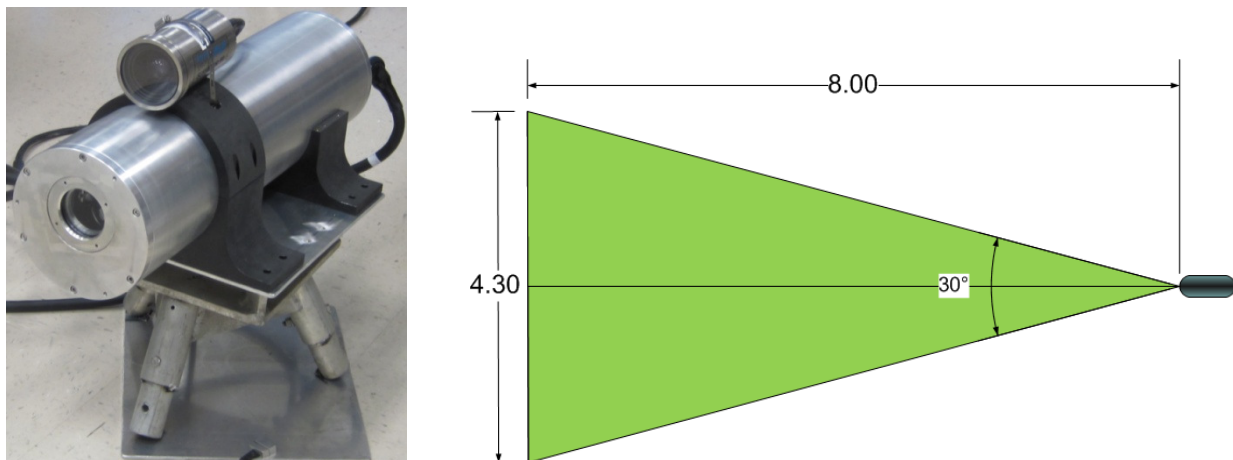


Figure 5. Prototype sensor mounted on a tripod with standard subsea camera mounted on top (Left). Programmable $\pm 15^\circ$ scan area in both azimuth and elevation provides 4.3m swath at 8m range (Right).

4 Pool Technology Trial

The 3D laser scanning sensor was tested underwater in early September, 2011 at the CDL facility in Houston, TX. This was the first test of the sensor completely submerged and operational. This section describes the experimental configuration and the test results for the trial.

4.1 Experimental Configuration

A 27-foot x 12-foot x 4-foot above-ground pool was used for the testing. Various targets were placed at one end of the pool and the laser sensor was placed at the opposite end. Typical range from sensor to target was approximately 5 - 7 meters.

The sensor was placed on the tripod as shown in Figure 6 below. On the cart to the left of the sensor is a lab power supply that provides the various voltage sources required by the sensor. This lab power supply was on the rolling cart next to the pool and connected to the sensor via standard subsea cables and Burton 5500 Series connectors. For the ROV tests in early 2012, a custom power board was integrated into the sensor to convert the ROV 26V DC power to the various required voltages of the sensor. The image on the right shows the sensor in the pool on the tripod with the subsea cables exiting the pool to the lab power supply.



Figure 6. 3D laser sensor on tripod connected to lab power supply on rolling cart (Left) 3D laser sensor and tripod in pool with subsea cables connecting to the lab power supply outside the pool (Right).

Communications with the sensor was established with an Ethernet connection through a standard Netgear Ethernet switch. A standard Dell laptop was used to control the sensor as well as process and visualize the resulting 3D datasets. Figure 7 shows the topside control laptop and the sensor control GUI on the smaller LCD screen. The larger LCD screen is connected to a standard underwater video camera (Bowtech Surveyor-SD with color and zoom) in order to view the underwater scene. This “control center” was placed next to the test pool; however the design allows for operation onboard a ship using the standard ROV Ethernet connections to control the sensor. Figure 7 also shows the test pool with the laser sensor illuminating targets on the opposite side of the pool.

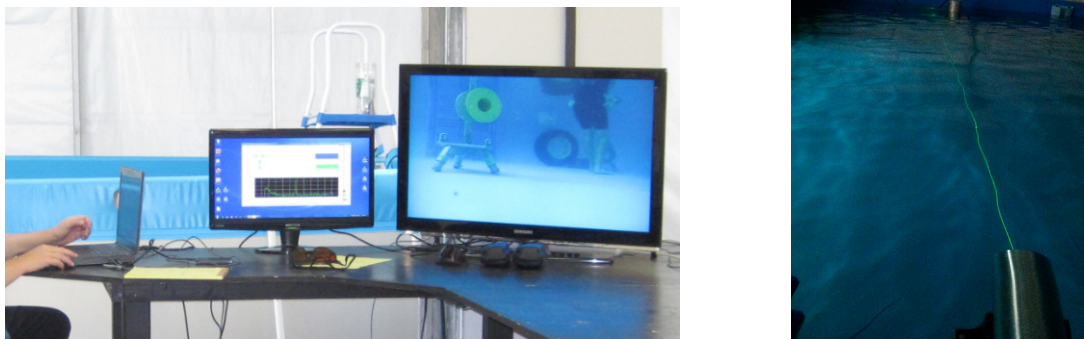


Figure 7. Topside control with a standard laptop through a standard Ethernet connection (Left) . Laser

sensor illuminating targets on the opposite side of the pool (Right).

4.2 Underwater Test Results and Discussion

The first underwater test performed was range (distance from the sensor) verification. To accomplish this verification a “base-line” wire was constructed with a marker placed every 1 meter as measured with a standard 5m metric tape measure. The sensor mirrors were adjusted so the laser was approximately level across the length of the pool. The first marker was then manually held against the sensor window and a tripod target (Figure 8) was moved to the different ranges as determined by the “base-line” wire. The range and range precision were measured at each location and compared with the base-line. Results are shown in Table 1.

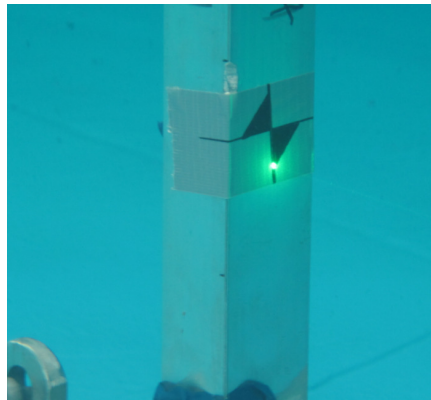


Figure 8. Tripod target used for range verification testing.

This data clearly shows that the prototype sensor was able to accurately measure range at 5 meters to within 3mm with a 6.3mm precision (1 standard deviation).

Table 1. Range Verification Data

Base Line Range (m)	Measured Range (m)	Delta (mm)	Range Precision (mm)
2.0	1.995	-5	6
3.0	2.996	-4	6
4.0	3.992	-8	7.5
5.0	5.003	+3	6.3

With basic range accuracy established, the next tests focused on scanning various objects at differing ranges in the pool. One goal of the scanning trial was to test the sensor on various materials, surfaces, object shapes, and ranges. Objects scanned include a rusted flange, a painted aluminum flange, small standard chain, a painted yellow pipe with a dent, a plastic crate, a standard automobile tire, and custom developed survey targets. All of the targets were submerged in the pool at specific locations where they were scanned individually and within groups.

Figure 9 (left) shows these various objects in the pool while performing a wide area scan. The laser is seen illuminating multiple objects during this wide angle scan as captured during a single camera integration time. The scan area was 29° in azimuth x 13.5° in elevation. The farthest object detected was the pool wall at 6.8m range. This equated to an approximately 3.52m x 1.61m scan area.

The actual data collection time for this scene was approximately 10 seconds. After the scan was completed, the resulting data was automatically transferred across the Ethernet connection through the switch to the control laptop. The transfer took less than 30 seconds. The data was then processed on the standard laptop to produce the image shown in Figure 9 (right). This data processing also took approximately 30 seconds. The 3D point cloud was then visualized in a color mapped view where colors changed based on their distance from the sensor. The visualization tools allow for pan, zoom and rotation. The processing and visualization were performed with 3D at Depth's proprietary software.



Figure 9. Multiple objects scanned at once. Image from HDTV underwater camera while performing a large area scan (Left). Resulting 3D data where color is mapped to range – blue is short range (Right).

In the processed data, color is mapped to range with blue being closest range and red being furthest range. The data set consists of a matrix of 200 x 200 data points. This wide area scan captures the entire scene to give the operator “situational awareness”. The operator can now focus in on different targets individually.

Some of the advantages and capabilities of a 3D laser scanner can be ascertained when looking at each target individually. First, a focused scan was performed on the closest flange, which was rusted and angled as shown in Figure 10. The flange was 13.5 inches in diameter and the 8 bolt holes were 7/8-inch in diameter. This target was selected for its various textures and colors that provided various reflectivity values for the laser sensor. This flange was 3.1 meters from the sensor.



Figure 10. Rusted, angled flange target (Left). The attitude is not identifiable with a straight-on orientation (Right).

The resulting 3D data is shown in Figure 11. The scan area was 7.2° in azimuth x 7.3° in elevation. At 3.1m range this equated to a scan area of approximately 0.4m x 0.4m and the resulting dataset was 200 x 200 points, which equated to a spatial resolution of approximately 2mm. With this resolution the 7/8 inch in diameter bolt holes were easily identified and could be measured.

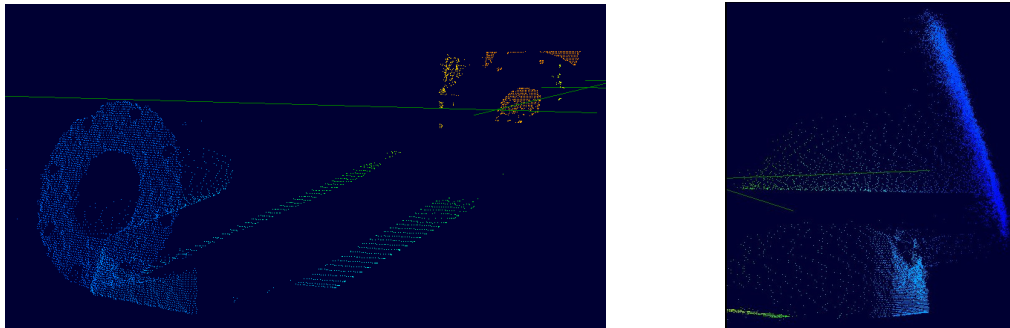


Figure 11. 3D Data of rusted flange. Isometric view shows the flange and shadow on the back wall (Left). Rotating the data 90° allows identification and measurement of features such as the flange attitude (Right).

Note the right image in Figure 10. This is the type of information one acquires with a 2D sensor (a standard camera). When looking straight-on to the flange one cannot detect the attitude. Unlike camera data, the 3D data from a single orientation can be viewed from multiple vantage points thus making the attitude easily recognized and measurable as shown in Figure 11.

A focused scan was next performed on the yellow flange (a common color for subsea assets) as shown in Figure 12. The flange was 10.0 inches in diameter and the 6 bolt holes were 0.5-inch in diameter. This flange was 5.3 meters from the sensor and close to the -15° side of the scene. Attached to the flange and hanging below it was a standard chain with 1-inch x 2-inch x 0.3-inch metal links.

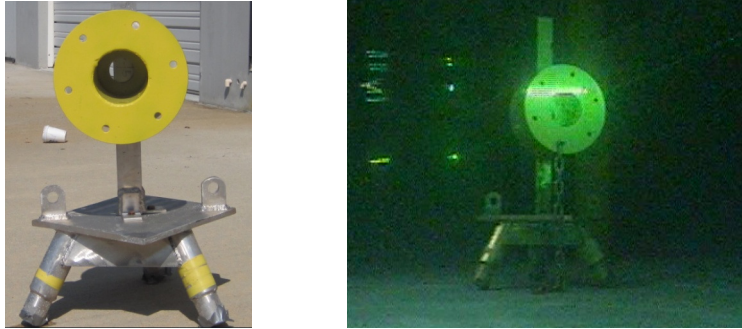


Figure 12. 10 inch diameter yellow flange (Left). Standard metal chain attached during the scan (Right).

The resulting 3D data is shown in Figure 13. The image on the left shows the initial scan. The scan area was 4.5° in azimuth x 5.5° in elevation. At 5.3m range this equated to a scan area of approximately 0.46m x 0.46m. The dataset was 200 x 200 points, which equated to a spatial resolution of approximately 2.3mm. With this resolution, the 0.5 inch diameter bolt holes were easily identified and could be measured, however the chain was not readily identifiable.

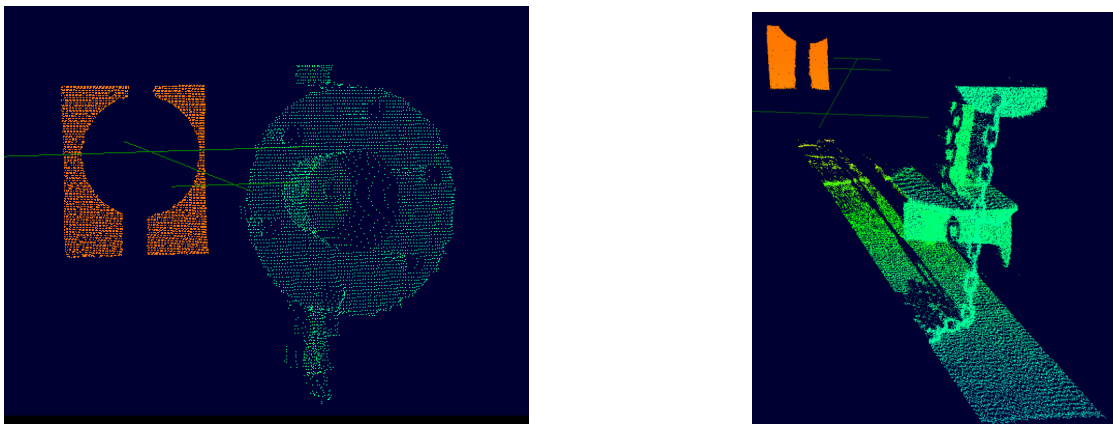


Figure 13. 3D data of yellow flange Lower resolution scan does not show chain detail (Left). Higher resolution scan does show chain detail (Right).

The image on the right shows a second, higher resolution scan. The scan area was 3.0° in azimuth x 7.0° in elevation. At 5.3m range this equated to a scan area of approximately 0.14m x 0.65m. This time the dataset was 400 x 400 points, which equated to a spatial resolution of approximately 0.35mm in azimuth. With this resolution the chain was now easily identifiable and could be measured.

On-the-fly operator control of scan area and scan resolution is a key benefit of this prototype sensor. One of the operational scenarios identified during these trials included the programmability of the sensor for “quick looks” at lower resolution; and then by viewing the resulting dataset, the operator can choose to scan specific areas at higher resolutions. This scenario would greatly benefit the ROV pilots while inspecting deep water assets.

A focused scan was next performed on a yellow pipe (a common color for subsea assets) as shown in Figure 14. The pipe was 8.0 inches in diameter and the center of the dent had two holes

– one approximately 3mm in diameter and one less than 1mm in diameter. The pipe was 5.9 meters from the sensor. Behind the pipe was a blue crate. The crate was used to simulate protective metal gratings or cages that are sometimes placed over subsea assets to protect them from fishing anchors, etc. The plastic crate would float, so it was wedged between the pipe and the pool wall for stability.



Figure 14. Scan of 8 inch diameter pipe (Left). Blue crate to simulate protective gratings (Middle). Scan with blue crate behind pipe (Right).

The resulting 3D data is shown in Figure 15. The image on the left shows an isometric view of the scan. The scan area was 4.0° in azimuth x 6.2° in elevation. At 5.9m range this equates to a scan area of approximately 0.41m x 0.64m. The dataset was higher resolution at 800 x 800 points, which equates to a spatial resolution of approximately 0.8 mm.

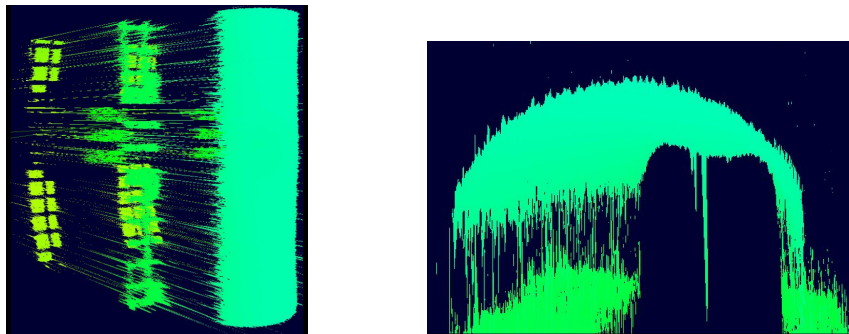


Figure 15. 3D data of 8 inch pipe at 5.9m range. Isometric view shows the pipe, crate, and pool wall all in one scan (Left). Same data rotated 90° reveals the 3mm and < 1mm holes in the pipe (Right).

Figure 15 (left) shows an isometric view of the scanned data. This demonstrates that in a single scan, the system acquired data from the pipe, the crate, and the pool wall. This simulated a pipeline inspection scenario in which the system could be used to inspect the pipe, a protective grating, and the seabed floor all in one pass. The distance of the pipe from the seabed could easily be measured and the pipe could be inspected at the same time.

Figure 15 (right) shows the same data rotated 90° . The spikes observed in the middle of the image equate to optical returns received from inside the pipe (longer range). This clearly identifies the 3mm and less than 1mm holes in the pipe. This demonstrates the capability of the system to detect small features at approximately 6m range and verifies the spatial resolution of the system. In the future, automatic feature recognition algorithms will be developed to automatically detect these types of features during a pipeline survey.

One goal of the prototype 3D laser scanning system is to take advantage of the large selection of standard software packages that have developed around the terrestrial 3D laser scanning industry. Therefore an important feature of our prototype is the ability to process the 3D point cloud using industry standard software packages. The 3D data from the pipe was exported into a trial copy of Leica's Cyclone LIDAR Processing product. The product was developed to process 3D point clouds into end user specific datasets for use in CAD and GIS applications. Using Cyclone, the point clouds were processed into a 3D surface model. This is shown in Figure 16 (Top). The dent in the pipe is clearly identifiable, but with the surface model additional operational data can be extracted. For example, most end users would want to know the measurable extent of the damage. Using Cyclone, a series of section cuts were created from the surface model with one cut at the apex of the dented section. The 3D surface model and section cuts were then exported into a .dxf format, and then imported into a trial copy of AutoCAD. Once in AutoCAD, measurements of the pipe and dent were made as shown in Figure 16 (Bottom).

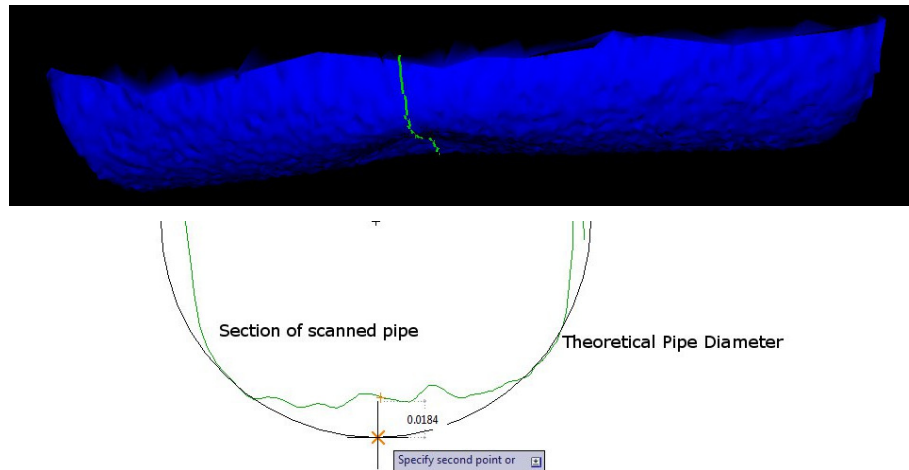


Figure 16. 3D point cloud data can be processed in standard software 3D model is generated in Leica Cyclone and a section cut is made at the dent (Top). The model and section cut are output into .dxf format and then imported into AutoCAD to make measurements of the pipe and dent (Bottom).

The pipe scan demonstrated the capability of the sensor to detect 1mm holes at a 5.9m range. It also demonstrated the ability to integrate the resulting datasets into standard software packages such as Leica Cyclone and AutoCAD in order to perform standard engineering analyses.

A focused scan was next performed on the standard car tire (Firestone Firehawk) as shown in Figure 17. The tire was 6.1 meters from the sensor. The scan area was 8.0° in azimuth x 6.0° in elevation. At 6.1m range this equated to a scan area of approximately 0.85m x 0.64m. The dataset was 600 x 600 points, which equated to a spatial resolution of approximately 1.4mm in azimuth. With this resolution the writing on the tire was clearly identifiable, along with the valve stem.

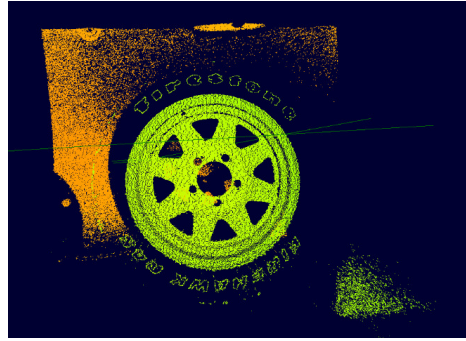


Figure 17. 3D data of Firestone Firehawk Tire at 6.1 meter range.

This object was scanned in order to test non-metallic materials. For this scan (at 6.1m range), the sensor did not register any returns from the black rubber, which is displayed as a dark area. The black rubber was not tested at closer range which could have yielded different results. The white lettering and the rim produce good signal returns and were clearly visible. The valve stem showed in the 11 o'clock position of the rim.

A final scan was performed of different example survey targets to perform a preliminary test of the sensor as a survey tool. Different survey targets were placed on a single platform as shown in Figure 18. The targets included a 7.42 centimeter diameter aluminum ball (painted with flat blue paint to reduce reflectivity) and two cylindrical reflective precision tape targets mounted on a vertical metal rod. The ball was chosen since spheres are commonly used reference survey points in terrestrial 3D laser scanning applications. The single point precision targets were chosen simply as a first test for this type of target.

The range to the survey targets was approximately 3.6 meters. The scan was 6.9° in azimuth x 10.32° in elevation. At 3.6m range this equated to an approximate $0.43\text{m} \times 0.65\text{m}$ scan area. The resulting data was 300×300 data points which equated to approximately 2.2mm resolution in elevation.

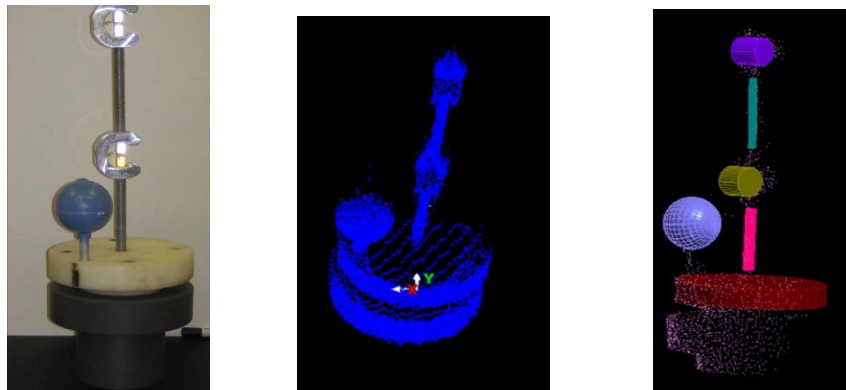


Figure 18. Tests on different survey targets. Photo of survey targets on docking platform (Left). 3D point cloud of survey targets (Middle). Solid model of survey targets (Right).

The survey targets were designed and assembled by UTEC Survey (Figure 18 Left). The target was then scanned in the pool and a resulting 3D point cloud produced (Figure 18 Middle). The point cloud was then processed by UTEC Survey into surface models (Figure 18 Right). The

single point precision targets did not produce adequate results during this first test, but the test sphere produced a solid geometry with a centroid location RMS value of 1.4mm. For survey applications a RMS value below 3 millimeter is desired.

This first test demonstrated the applicability of the underwater sensor as a survey tool with standard 3D laser scanning survey targets. Further design and testing is required to develop a single precision point target. This test again demonstrated the ability to transfer the point cloud data into industry standard software packages developed for terrestrial laser scanning.

5 ROV Technology Trial

The final technology trial of the phase 1 project was completed on February 16, 2012. The 3D laser scanning sensor was mounted on a Remote Operated Vehicle (ROV) and tested in a ROV test tank at the Schilling Robotics facility in Davis, CA. This was the first test of the sensor completely integrated with a work-class ROV and submerged for testing.

The goals for this final test of Phase 1 included:

- Integrating the sensor with a ROV and testing in a ROV test tank
- Operating the sensor's power and communications through the standard ROV channels
- In a ROV test tank, scanning multiple objects and comparing with actual object dimensions
- Viewing 3D data at the surface in real time

These goals were all achieved. This section describes the experimental configuration and the test results for this key technology trial.

5.1 Custom Power Supply

One of the primary enhancements for the ROV trial was the development of an onboard power supply. In the pool test, 3 different lab power supplies were used to generate the 7 different voltages required by the sensor. The approximate size of the power supplies were 17 x 22 x 5.5 inches. These lab power supplies were directly wired to the underwater cable that connected to the sensor. With this configuration the lab power supplies were left outside the pool to avoid additional packaging. This simplified the initial pool test so the basic functionality of the sensor could be verified and demonstrated.

For the ROV test a custom power supply was required to convert the 26V DC provided by the ROV into the 7 different voltages required by the sensor. The other major requirement of the power supply was size since the component would be packaged inside the sensor housing. Leveraging CDL, Inc.'s extensive experience with custom power supplies, a power board was developed that enabled the various electrical components to operate on ROV 26V DC power. CDL Inc. designed and built a custom power supply as cost share for this program which yielded a power supply 3.5 x 4 x 0.8 inch in size. This new power board is shown sitting on top of the lab power supply box in Figure 19 below.

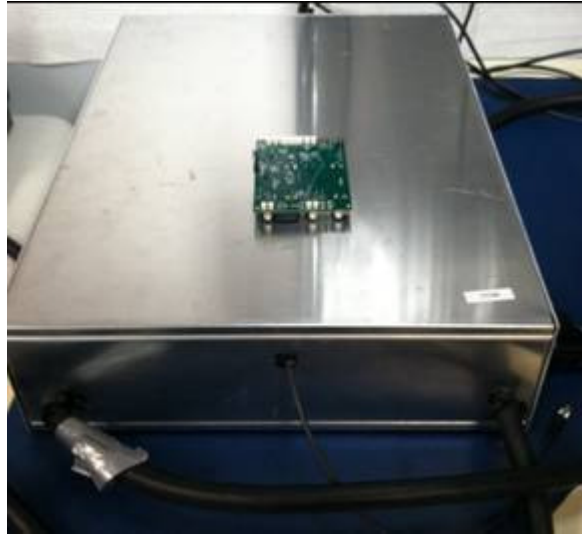


Figure 19. Custom power board sitting on top of the lab power supplies. The custom design enables integration of the power supply inside the underwater housing.

This power supply board enables soft start-up by allowing processor control of when certain subsystems are powered. The board also has a temperature and humidity sensor to monitor the environment inside the housing.

With this power board mounted inside the sensor, only a single connector is required to operate the sensor. A Burton 5500 series connector provides both power and Ethernet connection to the sensor and no other connections are required for operation.

5.2 ROV Experimental Configuration

The sensor was mounted to a Schilling Robotics Ultra Heavy-Duty (UHD) work-class ROV. This ROV is standard for operations at 10,000 foot depths. The laser sensor was directly mounted on the deck of the ROV as shown in Figure 20. A custom bracket supplied by CDL as cost share is used to mount the sensor directly to the ROV.

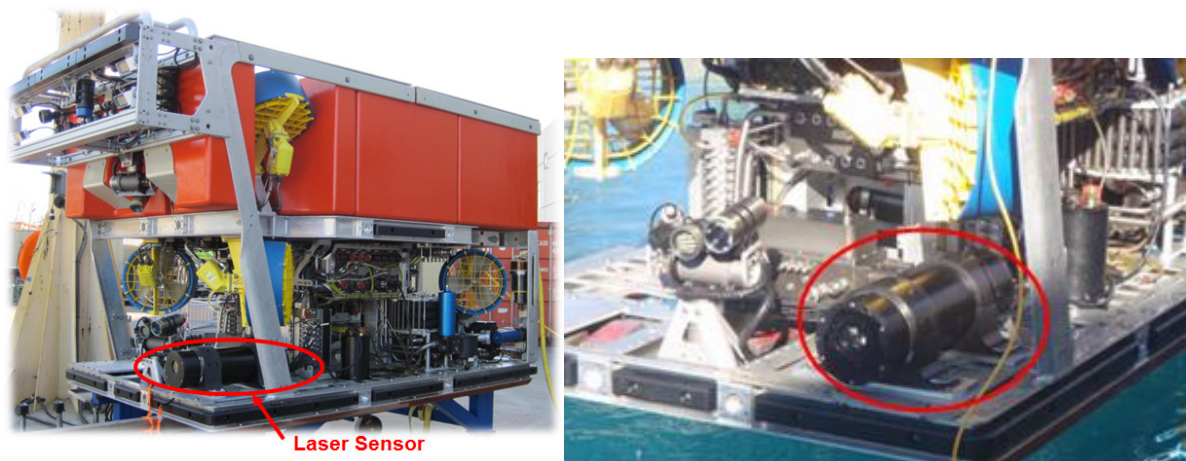


Figure 20. Laser sensor integrated with Schilling UHD ROV.

A single cable provides both power and Ethernet communication to the standard Schilling

Network Interface Module (NIM). This is shown more clearly in Figure 21 below. This single subsea cable provides both power and communications to the laser sensor.

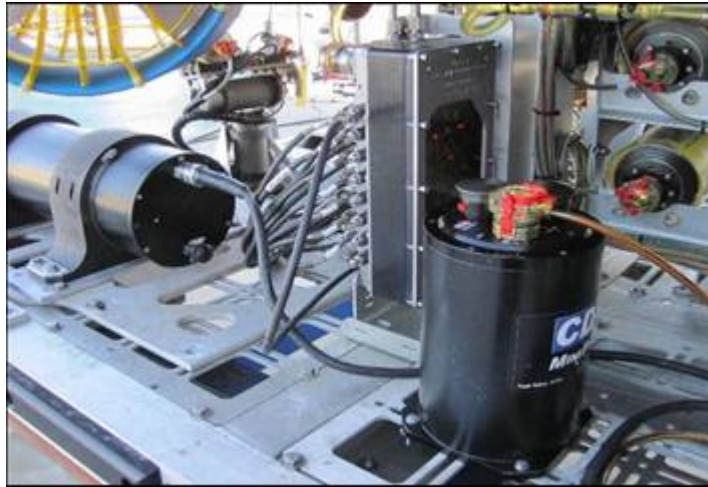


Figure 21. A single subsea cable provides both power and communications to the laser sensor.

The 26V DC power is a common voltage provided by the ROV from the AC high voltage power delivered down the tether. Communications to the sensor are managed by the ROV communications network and sent through the tether over a fiber optic link. For this test, 450 meters of tether were used between the topside control station and the ROV. The ROV and the Tether Management System (TMS) are shown in Figure 22 below.



Figure 22. Power and communications are delivered to the ROV through a 450 meter tether.

The laser sensor control laptop was placed in the Schilling control room and connected to one of their Ethernet switches. The laptop could then successfully communicate directly to the sensor using the Schilling ROV communications system through the 450 meter tether. The control

panel is shown in Figure 23 below.



Figure 23. ROV control center. Displays show two ROV mounted cameras, one tank mounted camera, one crane mounted camera, and the laser sensor control screen which is displaying data in the top right screen.

A hot stab panel was used as the primary target for this demonstration. Several dimensions were measured with a tape measure while the panel was still on land. The panel was then lowered with a fork lift into the pool. The panel is shown in Figure 24 below.



Figure 24. A Hot stab panel was used as the primary target for this test.

The ROV was then lowered into the tank with a crane to start the underwater imaging and measurements. Figure 25 below shows the ROV being lowered into the tank (left) and submerged in the tank while still connected to the crane (right).

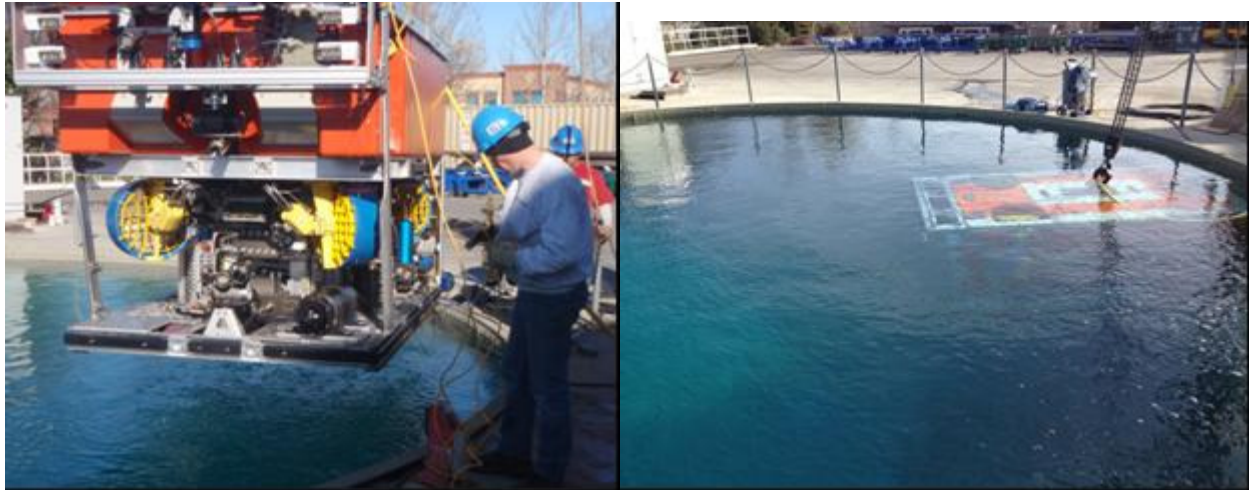


Figure 25. The ROV is lowered into the test pool with a crane (Left). The ROV is completely submerged and ready for test (Right).

The Schilling test pool is 36 feet in diameter and 18 feet deep. The distance from the laser sensor to the target panel was over 8 meters.

Note that the ROV, the TMS, the pool, the crane, the control center, the hot stab panel, and Schilling support personnel were all supplied to this program for free as cost share. This arrangement provided significant cost savings for the RPSEA program.

5.3 ROV Underwater Test Results and Discussion

The first underwater test performed was metrology verification. The goal of this test was to verify the measurement capability and accuracy of the sensor. For this test 3 bolts were used on the hot stab panel as verification points. The distance between these bolts were first measured on land with a standard tape measure as shown in Figure 26 below.

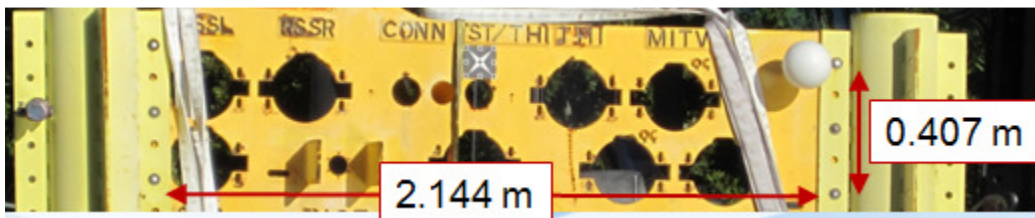


Figure 26. The distance between bolts was measured on land with a tape measure prior to lowering the hot stab panel into the pool.

Once underwater, the sensor was operated in static mode where the ROV was stationary and the laser was directed to each bolt as directed by the ROV underwater camera. Figure 27 shows a snap shot from the underwater camera monitor while the beam was being steered toward the bolt. *This was a key demonstration of an operational scenario for the laser sensor. Given the flexibility and ease of beam steering for this laser sensor, an operator can easily use the standard ROV camera to direct the laser to the point for making a desired measurement and then make that measurement instantly.*

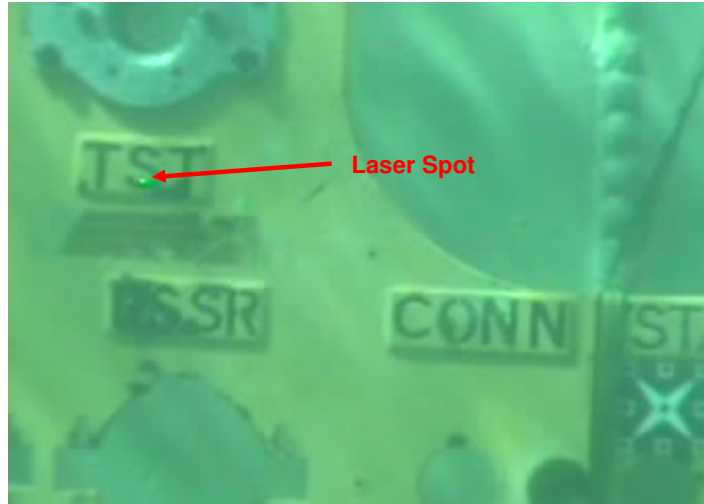


Figure 27. The laser spot is easily seen on the standard ROV camera monitor.

Once the laser was positioned on the bolt, range and bearing were measured and recorded. These measurements are made and recorded at each bolt. The sensor software then automatically calculates the distance between bolts. The results of this verification are shown in Table 2 below.

Table 2. Measurement Verification Data

Tape Measure Distance (m)	Underwater Measurement (m)	Delta (mm)
2.144	2.144	0
0.407	0.410	3

The results showed that at greater than 8 meter range the sensor measured distance between the bolts with 3mm accuracy. *To our knowledge this is the first time that 3mm measurement accuracy has been demonstrated at greater than 8 meter range for an underwater laser sensor mounted to a ROV.*

With accuracy established, the next test focused on scanning the entire hot stab panel. Figure 28 (left) shows the hot stab panel in the pool as seen from the main ROV camera monitor while performing a wide area scan. The laser cannot be seen during the scan due to the large amount of background (sunlight) in the pool. The ROV headlamps were turned on and also could not be seen on the target due to the large amount of sunlight. The pool tests were therefore performed with a larger amount of background light than is expected in underwater operations.

The scan area was 25° in azimuth x 18° in elevation. The farthest object detected was the pool wall at approximately 8.8 meter range. This equated to an approximately 3.9 meter x 2.8 meter scan area. *Note this 8.8 meter data correlates with the 9 meter range predicted by the theoretical models presented in Section 2.* The processed 3D data is shown in Figure 28 (right).

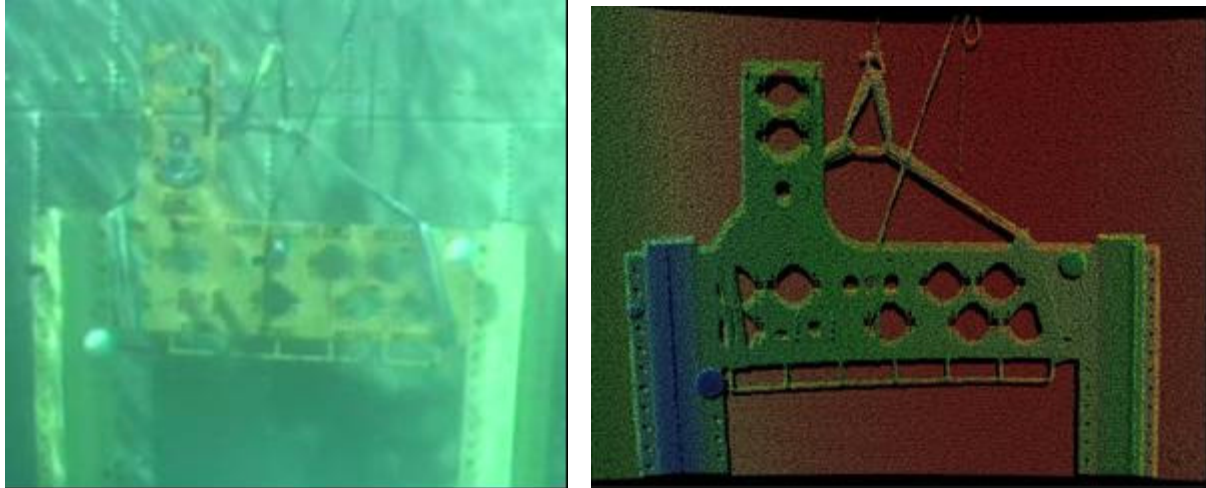


Figure 28. Hot stab panel as viewed from main ROV camera monitor (Left). Processed 3D data from laser scanner with color mapped to range – red is furthest distance (Right).

Note the laser scanner detected the yellow panel, the gray and white lifting straps, and the pool wall. Also note that the laser sensor performed as predicted in Section 2 with a large amount of background light, demonstrating that the sensor is robust in the presence of ROV headlamps.

During the scan, data was automatically transferred across the 450 meter tether through the fiber optic link to the control laptop. Since the data transfer was occurring simultaneously with the scan, the data was ready to be processed on the control laptop only a second after the scan completed. This is a significant improvement over the pool demonstrations in September 2011. The data was then processed on the standard laptop to produce the image shown in Figure 28 (right). The entire process from performing a scan to viewing data on the screen took less than 1 minute. The 3D point cloud was then viewed with range mapped to color and could be rotated, panned and visualized. This was again performed with 3D at Depth's proprietary software. Figure 29 below shows the same data set rotated to view the profile (range data). With this view the curve of the pool wall is easily seen, along with other features.

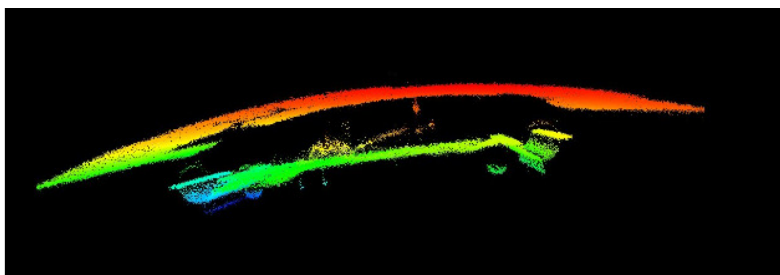


Figure 29. Profile view of hot stab panel using the same data from Figure 28.

In the processed data, color is mapped to range with blue being closest range and red being furthest range. The resulting data set is 400 x 400 data points. This wide area scan captured the entire scene to give the operator “situational awareness”. The operator could then visualize the resulting data and identify specific areas for higher resolution focus.

Figure 30 (Left) shows a close-up view of two fins on the hot stab panel before being placed in the pool. These fins are 20.5 cm apart and 17.8cm deep. Figure 30 (Right) shows the fins as seen from the ROV main camera. Note the image is not clear and with the ROV's head-on view

the depth of the fins is difficult to infer. The shadow of the fins caused by the sunlight above is the only indication of the existence of the fins from this straight-on perspective. When operating with ROV headlamps mounted close to the camera, these shadows would not be seen making it very difficult to even see there is a feature with depth. Also note the lettering below the fins “PIGE”. The lettering has a depth of approximately 8 mm.



Figure 30. Two fins on the hot stab panel as seen in air (Left) and by the ROV main camera (Right).

A more detailed scan of this area was performed with the laser sensor. The scan area was 3.0° in azimuth x 3.0° in elevation. At 8.2 meter range this equated to a scan area of approximately 0.43 meter x 0.43 meter. The dataset was 400 x 400 points, which equated to a spatial resolution of approximately 1.1mm at 8.2 meter range. The resulting dataset is shown in Figure 31 below.

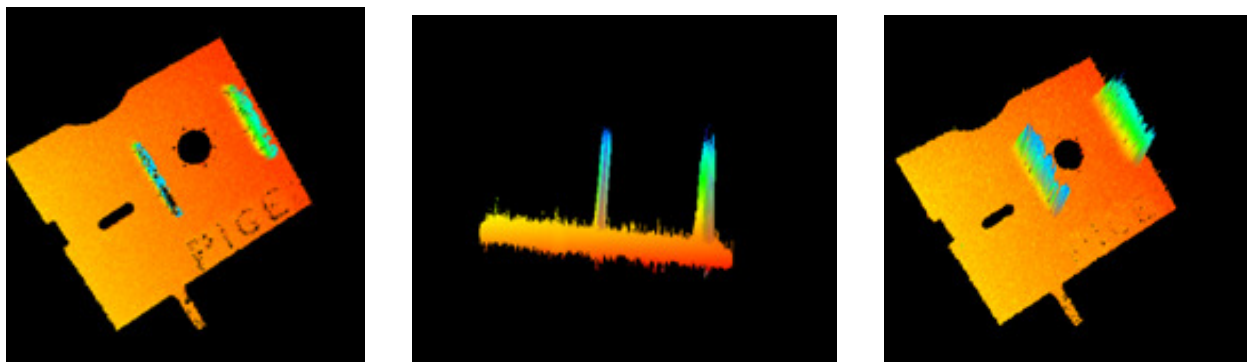


Figure 31. A single 3D scan of the fins easily shows the depth of the fins along with the writing below.

Figure 31 (Left) shows the straight-on view of the dataset. The depth of the fins is identified by the blue color (blue is mapped to closer range than red). Note in this view the lettering “PIGE” is identifiable. Figure 31 (Middle) shows a profile view of the dataset. To obtain this view, the same data was simply rotated in the 3D at Depth data viewer. From this view the depth of the fins is easily identifiable and can be measured. Figure 31 (Right) is an isometric view of the dataset to give another perspective of the object. The height of the fins and the distance between the fins was verified to within 2mm accuracy while operated in static mode and the ROV was stationary. This is another example of the flexibility of the laser sensor which allows operators to scan different areas with varying resolutions depending upon the objects and problems being

addressed.

Another observation worth mentioning was the presence of particles in the Schilling pool. While it was a pool that is filtered, there was still a significant amount of debris floating in the water. When watching the ROV video monitor, particles are constantly seen floating by the camera. Figure 32 attempts to capture some of those objects in a still frame. Every white spot or streak seen in the photo is a particle that is floating by the camera. While it is not very obvious in a single frame, it is very obvious when viewing live on a screen. This observation gave further proof of the ability of the sensor to perform in non-laboratory conditions.



Figure 32. Still-screen capture of the laser sensor from the ROV main camera showing some of the particulates in the water. Every white spot and streak is a particle.

These tests concluded the testing required for the Phase 1 activities. ***Additional tests and activities were performed beyond Phase 1 requirements to increase the productiveness when starting Phase 2. These additional activities were achieved without an increase in cost of the Phase 1 program.***

Another trial copy of Leica Cyclone was obtained for these tests. Since it was a trial copy, it was only available for 2 weeks of time, thus limiting the amount of development, processing, and debugging that could be achieved. A full version of Leica Cyclone will be purchased at the start of Phase 2. Using Cyclone, the 3D point cloud of the hot stab panel was processed and is shown in Figure 33 below.

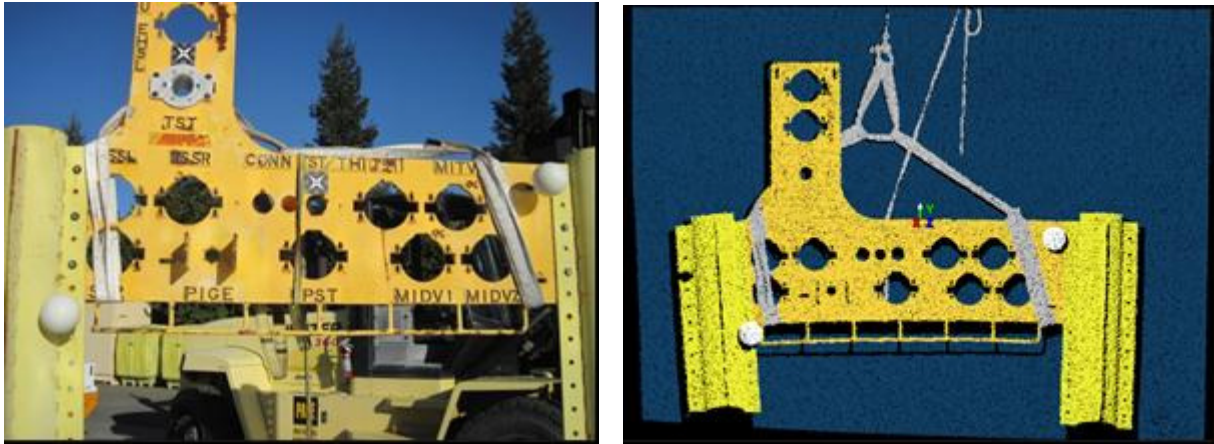


Figure 33. Post processing of 3D data using Leica Cyclone.

Leica Cyclone is used to process the point cloud, convert groups of points into standard surface models (spheres, surfaces, and cylinders) and to make measurements on these models. Figure 34 below shows the hot stab panel in Cyclone with the supports converted into model cylinders and the spheres converted into model spheres.

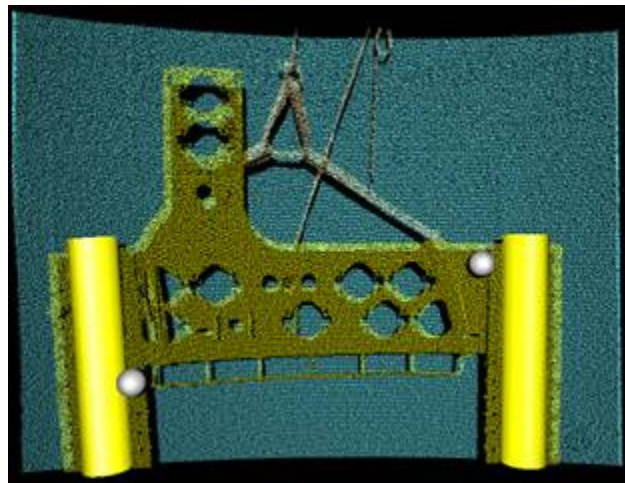


Figure 34. Hot stab panel data in Cyclone with the supports converted into model cylinders and the spheres converted into model spheres.

Some discrepancies were found between solid model measurements and physical measurements that indicate an error somewhere in the overall setup of the targets or in the data processing workflow. This will be addressed during Phase 2 with a full license of Leica Cyclone and the continued research on metrology processes and targets.

One of the key activities of Phase 2 is to perform scans of objects from a moving platform as this will greatly expand the usable platforms and operational scenarios for the sensor. The first step for solving this problem is to use the navigation data from the ROV to assist in the data processing. To jump start this activity for Phase 2, 3D at Depth collected navigation data from the ROV and from the CDL miniPOS2 while performing all scans. Using this ROV test opportunity to acquire navigation and scan data now allows for earlier algorithm development during Phase 2.

Figure 35 below provides a visualization of the problem. For this data collection the ROV was

released from the crane and placed in station keeping mode. Station keeping mode is a standard option for Schilling ROVs where the operator places the ROV in a desired location and then it automatically attempts to keep itself in that particular location. While the level of station keeping accuracy is acceptable for most ROV operations and camera viewing, it was not expected to be accurate enough for precise laser scans. Figure 35 (Right) shows the laser data captured while in station keeping mode.

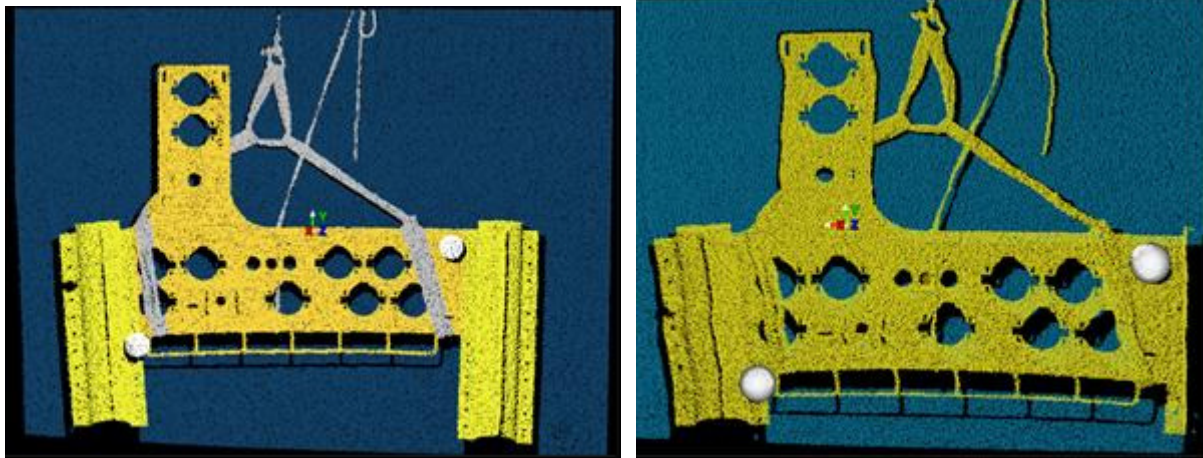


Figure 35. Data was collected and processed while ROV was static (Left) and while the ROV was in station keeping mode (Right).

In particular, notice the “wavy” fins on the left stand and the wavy edges of the hot stab panel when comparing the image on the right to the image on the left. One of the main goals of Phase 2 is to address this issue and to integrate data from the INS to apply corrections to the resulting datasets.

In summary, at the conclusion of the ROV technology trial, all goals for this final test of Phase 1 were achieved:

- Integrating the sensor with a ROV and testing in a ROV test tank
 - Integrated with Schilling UHD ROV
- Operating the sensor’s power and communications through the standard ROV channels
 - Operated through 450 meters of subsea tether
- In a ROV test tank, scanning multiple objects and compare with actual object dimensions
 - Maximum error = 3 mm
- Viewing 3D data at the surface in real time
 - 3D data captured, processed and viewed in less than 1 minute

Note that by the end of the demonstration the sensor system had operated more than 8 hours a day for two days in a row without any issues. In addition, after several cycles of being lowered into and out of the tank, the sensor did not have issues related to calibration. These both attribute to the robustness of the sensor design and its readiness for the open water trials at the beginning of Phase 2.

6 Reliability Testing

In addition to performance testing, preliminary reliability testing was performed on the prototype

sensor to test survivability in expected deployment environments. Tests included Operating Temperature, Storage Temperature Cycling, Vibration tests, and Shock tests. As with any optical sensor (especially laser based sensors) the primary concern is the moving or shifting of optics in the optical train due to vibrations or thermal changes. With laser based sensors, very small movements of the optics just due to thermal expansion /contraction can cause optical misalignment and thus serious performance degradation if not designed properly. 3D at Depth performed both thermal & mechanical Monte Carlo tolerance analysis of the optical system prior to construction in an attempt to generate a robust design. These reliability tests are required to verify the design.

Reliability testing was performed in October 2011. Prior to any tests, the sensor was thoroughly visually inspected for any particles, debris, wire locations (pinch points), and rub points. In addition all fasteners and cable connectors were tightened to their appropriate level. A functional test was then performed with a calibrated target at 30-foot range in air and the received signal was recorded at 1.7V.

6.1 Thermal Testing

Figure 36 below shows the sensor in a Cincinnati Sub-Zero environmental chamber model Z-32-2-2-H/WC. The chamber has a window which allows for functional testing of the sensor before, during, and after thermal fluctuations. The sensor lab power supply and control computer are outside the chamber as shown in the image on the left. The subsea cables are connected to the sensor through a port in the side of the chamber.

The temperature inside the sensor was measured at one of the critical components (the receiver electronics). In order to make this measurement the system had to be powered, however the powered sensor would generate heat. Therefore the sensor was left off and allowed to soak at each temperature for at least one hour prior to sensor turn-on and temperature check to ensure the inside of the sensor was reaching the chamber temperature.



Figure 36. Window in thermal chamber allows functional testing of the sensor during thermal tests.

The primary functional tests performed included:

- 1) Basic functionality / communication established
- 2) Received signal power level

3) Pointing stability

To make these measurements a temporary target wall was installed approximately 5.5m from the sensor. For initial setup, nine points were marked on the target as initial starting points for beam location and return signal amplitude. The nine locations were set to test the maximum scanner angle allowed as defined by the 5.5m distance and sensor height in the chamber. Maximum elevation angles were from 11° to -5°, while maximum azimuth angles were from -15° to +15°.

6.1.1 Operating Temperature

The primary goal of the operating temperature tests was to verify system functionality and basic performance at expected operating temperatures. During the pool trials in Houston, the standard water temperature was approximately 22° C, so the upper end of operational temperatures had already been tested. Since the sensor is designed for 3000m operation, cold water operation needed to be verified. Tests were performed at 22° C, 5° C, and -1° C chamber temperatures. The sensor was allowed to soak for 2 hours at the -1° C chamber temperature prior to performing functional tests.

Results showed the system operated normally at all temperatures and strong signal levels were recorded at all 9 locations. It was also revealed that the test setup was not adequate for precise evaluation of the sensor. Upon inspection during the tests it was observed that the temporary target wall moved based on air currents in the room and whenever a person walked by the target. This created fluctuations in both the signal level return and the exact location of the beam at each of the 9 angles. In the future this test must be performed in an environmental chamber whose window has clear line-of-site to the building wall. However, this “problem” showed the sensitivity of the sensor to detect millimeter scale movements of the target caused by air currents.

Despite this test setup variation, the maximum angular displacement was found to be approximately 909 μ rad (approximately 0.052°) and the maximum signal level variation was found to be a twofold increase in signal level during the -1° C test as compared to initial conditions.

6.1.2 Thermal Cycling (Storage Temperature)

The primary goal of the preliminary thermal cycle test was to shock the sensor with temperature extremes to test optical alignment and solder joint robustness. In addition, this test assessed conditions the sensor could experience while in storage. One sub-system component was not guaranteed below 0°C prior to this test, so -1°C was set as the limit for this test in order to not risk the ROV tests in early 2012. In the future, this component will be replaced and thermal cycling will occur from 60°C to -20°C.

The thermal test consisted of transitions from 60°C to -1°C, with a 2°C/min transition and a one-hour soak at each temperature extreme. This equated to five cycles for a full 16 hours of temperature testing overnight. The chamber then soaked at 10°C for 2.5 hours prior to performing functional test.

Results again showed the system operated normally after a full night of temperature cycling and strong signal levels were recorded at all nine locations, despite the target induced variations. The maximum angular displacement was approximately 4.2mrad (approximately 0.24°) and the maximum signal level variation was an approximately 1.8 times increase in signal level compared to the initial conditions. Note this is after the temporary target wall was setup for a

full night.

In summary, the system survived and showed no performance issues during operating and storage temperature testing.

6.2 Shock and Vibration Testing

Following the temperature tests, the system was then subjected to shock and vibration testing. Figure 37 below shows the sensor mounted on a Dynamic Solutions Vibration Shaker Model DS-15400VH122-70. The prototype sensor was monitored through multiple Dytran Single-Axis Piezoelectric Accelerometers (Model 32225F1) with at least one mounted in each orthogonal axis of motion, along with a control accelerometer mounted on the table.

The table vibrates in one linear direction so the sensor must be rotated to test each axis. In Figure 37 below the test direction is perpendicular to the optical window. To test the vertical axis the sensor base is left as shown in Figure 37, however the sensor is rotated 90° within the black clamps.

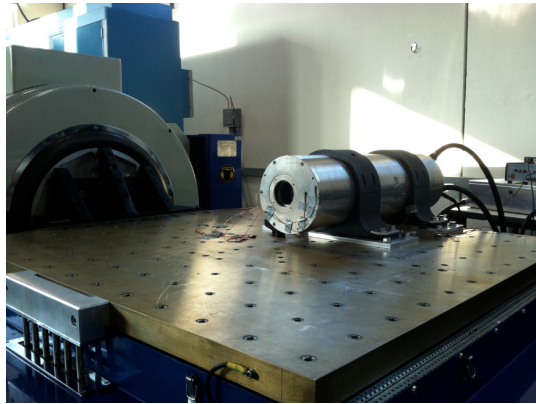


Figure 37. Sensor mounted on vibration table for shock and vibration testing.

Both vibration and shock testing were performed in each axis prior to moving the sensor to the next test axis. All fasteners used to attach the sensor to the vibration table were tightened to a specified torque prior to each test. Basic functional testing was performed after each test that included pointing the beam to three different locations on the building wall and recording the location and return signal voltage.

6.2.1 Vibration Testing

The primary goal of the vibration testing was to not only verify basic survivability, but also to look for any resonant vibrations that could become long term issues. Vibration testing was performed in accordance with the Department of Defense Military Standard for Mechanical Vibrations of Shipboard Equipment (MIL-STD-167-1A). For this preliminary testing, the Exploratory Vibration Test (5.1.2.4.2) was performed to search for resonances. The test was from 4 to 33Hz with approximately 15 seconds at each frequency.

Figure 38 below shows two example accelerometer outputs while testing the vertical axis. The graph on the left shows an in-plane accelerometer matches the input signal with no resonance. The graph on the right shows an out-of-plane accelerometer is well below the demand and shows no resonance structure for inside the sensor. This type of data was recorded for every

accelerometer for each axis of testing.

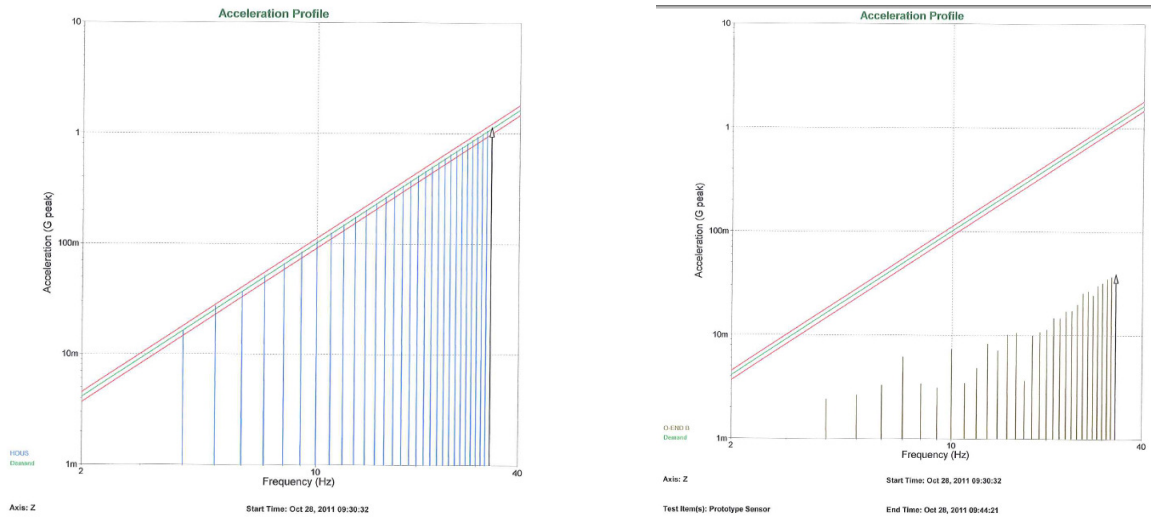


Figure 38. Example accelerometer output during vibration testing for the Z-axis. Accelerometer is in-plane with the Z-axis and matches the input accelerations without resonance (Left). Accelerometer is out-of-plane with the Z-axis and shows no signs of resonance (Right).

In addition to the accelerometer data, the same basic functional tests were performed as for the thermal chamber tests. These tests were performed against a nearby building wall. However, after moving the vibration table does not return to its exact location, thus skewing the angular tests of the sensor. Despite this issue, the maximum angular displacement was found to be approximately 360 μ rad (approximately 0.021 $^\circ$) and the maximum signal level variation was found to be an approximately 27 percent increase in signal level compared to the initial conditions.

6.2.2 Shock Testing

The primary goal of the shock tests was to not only verify basic survivability, but also to look for any resonant vibrations that could become issues. Shock test conditions were three pulses per direction along each of six principle directions, 1/2 sine shock at 3g acceleration and 11ms nominal duration.

Figure 39 below shows example accelerometer outputs while testing the vertical axis. The graph on the top is the drive input. The bottom graph shows the accelerometer outputs for seven different accelerometers. The in-plane accelerometers follow the drive shock pulse very closely, while the out-of-plane accelerometers remaining basically flat. No resonance features are observed. This type of data was recorded for each axis of testing.

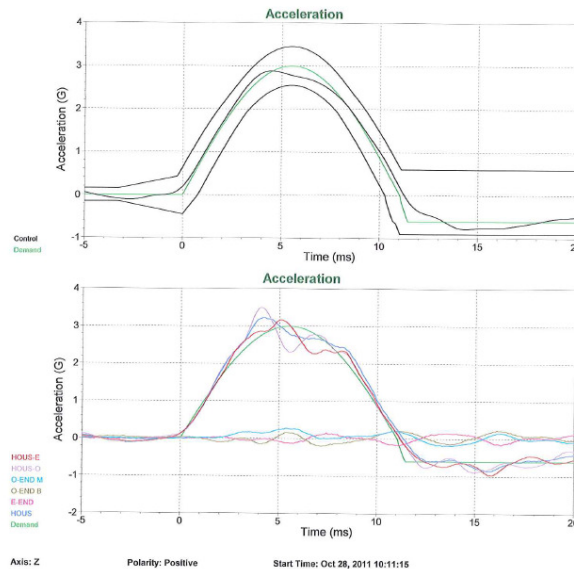


Figure 39. Example accelerometer output during shock testing for the Z-axis. Shock pulse is within the accepted tolerances (Top). Outputs from seven accelerometers show no resonance features (Bottom).

In addition to the accelerometer data, the same basic functional tests were performed as for the vibration tests. These tests were performed against a nearby building wall. However, after moving the vibration table does not return to its exact location, thus skewing the angular tests of the sensor. Despite this issue, the maximum angular displacement was again found to be approximately $360\mu\text{rad}$ (approximately 0.021°) and the maximum signal level variation was found to be an approximately 33 percent increase in signal level compared to the initial conditions.

In summary, the system survived and showed no resonance or performance issues during both vibration and shock testing.

6.3 Final Inspection

After all tests, the sensor was thoroughly visually inspected for any particles, debris, wire locations (pinch points), and rub points. Inspection revealed that two wires were subjected to very minor pinching; all fasteners and connectors were still tight; and a few points of physical rubbing were observed inside the sensor that caused small chips of the aluminum housing to be scraped off. The physical rubbing during vibration and the minor wire pinching are both being addressed in the next design.

In addition, the same functional test was again performed with a calibrated target at 30-foot range in air and the received signal was recorded at 1.7V (unchanged).

6.4 Transit Case Testing

In addition to reliability testing of the sensor itself, the performance of the transit case was also tested. The transit case is a key component of the system whose performance must be verified to ensure reliable operation of the sensor. It is often overlooked during the development of a new technology.

To determine test conditions, we investigated both the International Safe Transit Association Requirements for Parcel Delivery (3A) and the military standard MIL-STD-810G / Transit Drops. After reviewing both standards, it was determined that for the weight and size of our transit case, the MIL-STD-810G was more stringent with a 24 inch drop height.

The sensor was monitored using three accelerometers (one in each axis) attached to the window side of the housing as shown in Figure 40 below. An accelerometer was also mounted outside the transit case in the axis of impact as a control. For these tests, only the housing was included in the drop tests. The internal components were all removed to reduce risk to the sensitive hardware.



Figure 40. Housing in transit case with three accelerometers attached (one in each axis).

The prototype sensor was monitored through multiple Dytran Single-Axis Piezoelectric Accelerometers (Model 32225F1) with one mounted in each orthogonal axis of motion. The signals were captured with a Vibration Research Transient Capture Controller (Model VR9500). The drop tests were performed on a MT Labs Package Drop Device (Model AD500). The transit case is a Pelican Case Model 1780. All of these components are shown in Figure 41 below with the transit case ready for a 24 inch drop test.

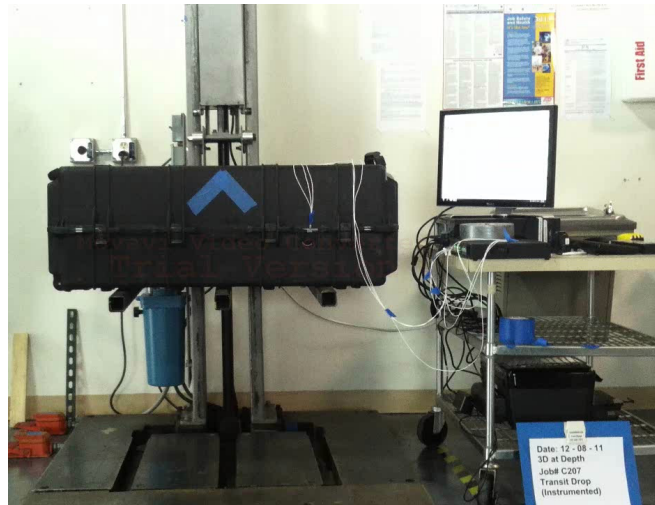


Figure 41. Transit case and housing instrumented and ready for 24 inch drop test.

Figure 42 below shows example accelerometer outputs while testing in the configuration shown in Figure 41. The graph on the top left is the control accelerometer showing a 300g shock external to the transit case. The bottom right graph shows the accelerometer output for the housing in the direction of the drop. This type of data was recorded for each axis of testing.

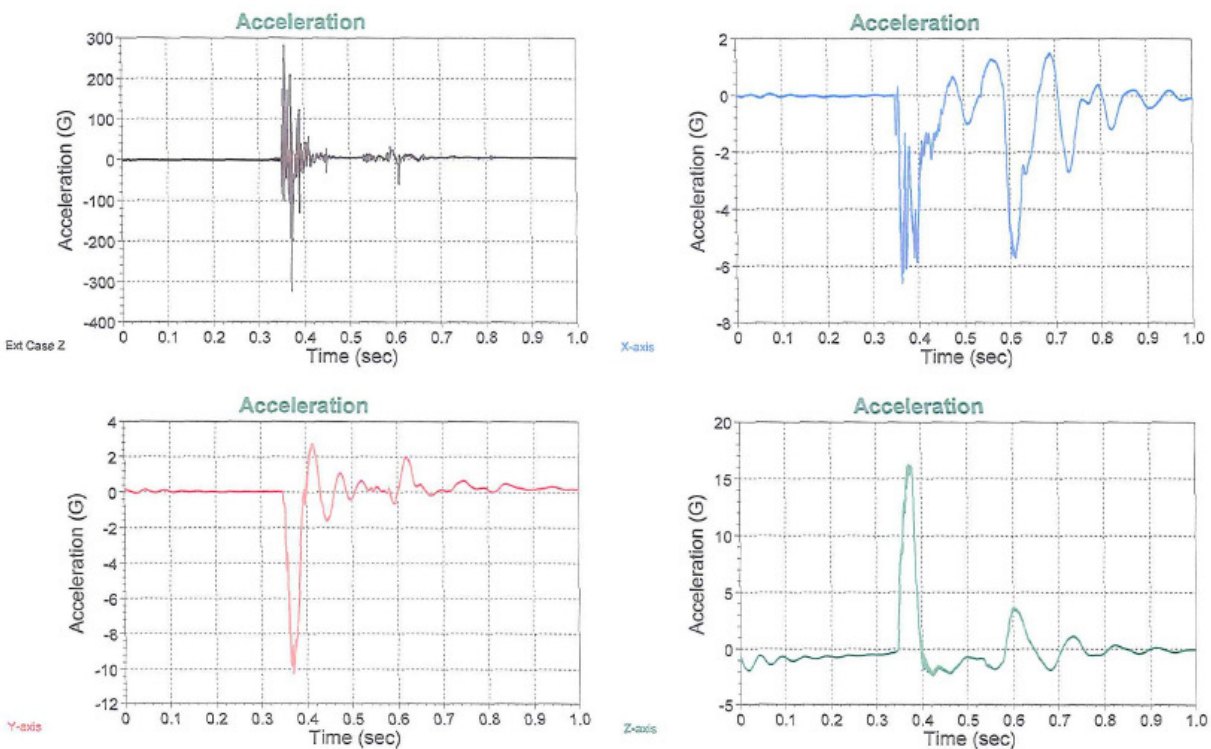


Figure 42. Example accelerometer output during drop tests. This data shows a successful packaging test where proper packaging reduced the shock from 300g to 16g.

The data in Figure 42 shows that proper packaging can reduce the shock from 300g to 16g in the direction of impact. This data is from drop number eight, and reflects modification to the packaging learned in the first seven drops.

Figure 43 shows similar data for a 24 inch drop onto the smallest end of the transit case. Note the shock in this axis approaches 1000g external to the case and 27g on the housing in the direction of the drop.

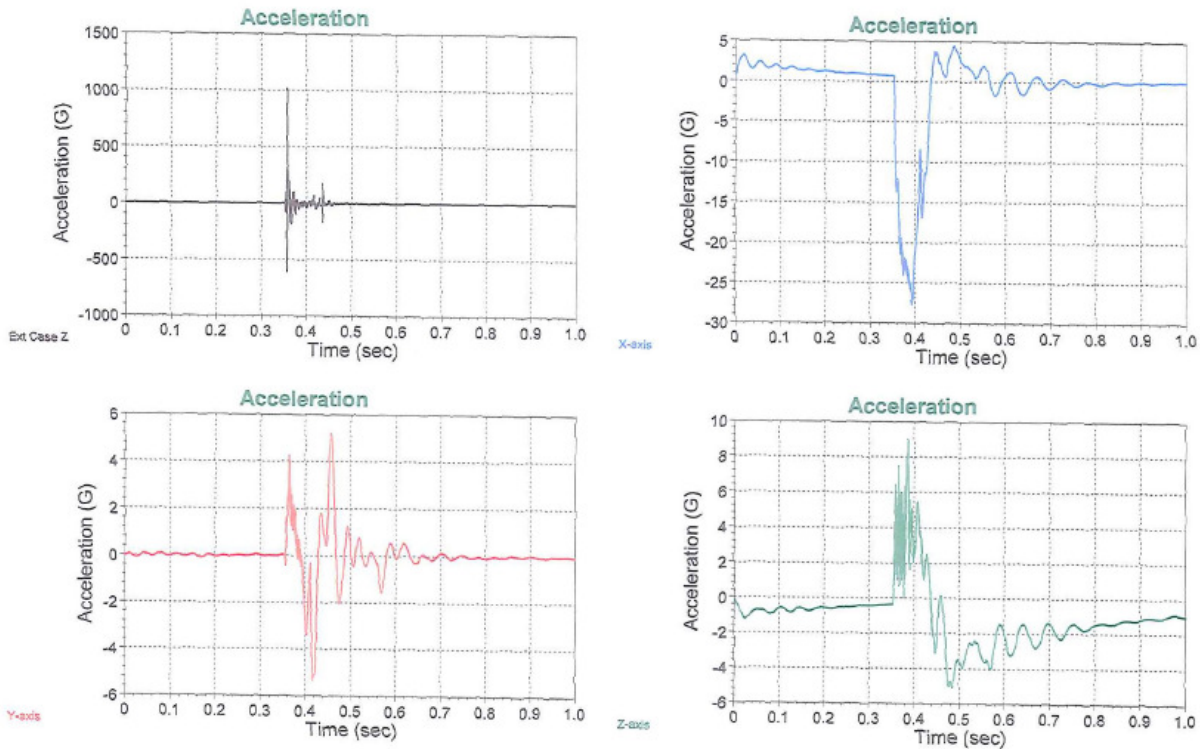


Figure 43. Example accelerometer output during drop tests. This data shows 1000g shock when dropped on the small end of the transit case.

The goal for our transit case is to reduce shock to the housing below 20g. The current transit case does not provide this level of protection in all axes. Therefore a new transit case or internal packaging is required prior to shipping with a commercial carrier to ensure proper protection for the sensor. This will be further investigated during Phase 2.

7 Conclusions

Three dimensional laser scanning offers a new capability to the industry for quickly capturing survey quality data for construction, repair, and maintenance. This ability to quickly capture high resolution 3D models provides a key component of integrity management for a variety of production assets.

In this project we further developed hardware and software for an underwater 3D laser scanning sensor that provides resolutions similar to terrestrial systems at ranges up to nine meters. Theoretical models were presented that predicted approximately 20dB SNR signal levels at 9 meter range in Jerlov Type II oceanic water. Underwater tests were first performed in a pool with strong signal returns at 6.8 meter range from the pool wall. The experimental ranges were therefore limited by the size of the pool. 3D at Depth is implementing more sensitive receivers in the next RPSEA phase to further increase range and enable operation in more turbid

conditions. The next phase will also entail more detailed testing of the system in turbid waters.

The range precision of the sensor was characterized during the first pool tests and at 5 meter range produced a range error compared to the baseline of 3 millimeters and a range precision of 6.3 millimeters. Multiple objects were scanned to test different materials including rusty metal, shiny metal, yellow paint, blue plastic, black rubber and white rubber. All materials produced strong returns except for the black rubber at 6.1 meter range. The black rubber was not tested at closer ranges. Testing of all materials will continue with the more sensitive receiver during Phase 2. This will determine at what range a black rubber target can be imaged.

Spatial resolution was verified through detection of a less than 1mm hole in a dented pipe at 5.9 meter range. In the future automatic feature recognition algorithms could be developed to automatically detect these types of features during a pipeline survey. A single data acquisition was performed where the system acquired data from an 8-inch pipe, a crate, and a pool wall. This demonstrated that in a pipeline inspection scenario the system could be used to inspect the pipe, a protective grating, and the seabed floor all in one pass. The distance of the pipe from the seabed could easily be measured and the pipe could be inspected at the same time.

One goal of the prototype 3D laser scanning system is to take advantage of the large selection of standard software packages that have developed around the terrestrial 3D laser scanning industry. We demonstrated the ability to integrate the resulting datasets into standard software packages such as Leica Cyclone and AutoCAD in order to perform standard engineering analyses.

In a second test, the sensor was successfully integrated with a Schilling Robotics UHD ROV and operated in a ROV test tank. The sensor operated through standard ROV power and communications systems which included 450 meters of subsea tether from the ROV to the topside high voltage power supply and control center. Scanning and data transfer occurred simultaneously which allowed the 3D data to be collected, processed and viewed in less than 1 minute. The furthest object detected in this test was the pool wall at 8.8 meter range. ***Note this 8.8 meter data correlates with the 9 meter range predicted by the theoretical models presented in Section 2.***

In a ROV test tank, multiple objects were measured at greater than 8 meter range and compared with actual object dimensions. The maximum error recorded when compared with the measurement made in air was 3mm. ***To our knowledge, this RPSEA program enabled a world's first demonstration of 3mm measurement accuracy at greater than 8 meter range for an underwater laser sensor mounted to a ROV.***

This was performed by viewing the laser spot on the target using the standard ROV camera. The operator then easily moves the laser spot to the desired location on the target and makes a measurement instantaneously. This was a key demonstration of an operational scenario for the laser sensor. Given the flexibility and ease of beam steering for this laser sensor, an operator can easily use the standard ROV camera to direct the laser to the point for making a desired measurement and then make that measurement instantly.

Along with detailed scans, a wide area scan with multiple targets at multiple ranges was demonstrated. The scan area was 25° in azimuth x 18° in elevation. The farthest object detected was the pool wall at 8.8m range. This equated to an approximately 3.9m x 2.8m scan area. Therefore on-the-fly operator control of scan area and scan resolution was successfully

demonstrated. Operationally, the sensor can be optimized for fast scans of large areas and then when areas of interest are identified; highly detailed scans can be performed at much higher resolutions (at the cost of scanning speed).

The ROV tests were performed during the day with a high level of background sunlight. The background sunlight was stronger than the ROV headlights as viewed by the ROV cameras. By performing the ROV tests in the presence of strong background sunlight, ***we demonstrated the robustness of the sensor to background light levels higher than ROV headlamps.***

Additional tests and activities were performed beyond Phase 1 requirements to increase the productiveness when starting Phase 2. ***These additional activities were achieved without an increase in cost of the Phase 1 program.*** These included importing data into a trial version of Leica Cyclone and converting the point clouds into solid models. In addition, navigation data was acquired simultaneously to laser scans while the ROV was in station keeping mode and while moving. The early acquisition of this data will be used to jump-start the Phase 2 algorithm development to enable laser scanning from moving platforms.

The ROV, the TMS, the pool, the crane, the control center, the hot stab panel, and Schilling support personnel were all supplied to this program for free as cost share. This arrangement provided significant cost savings for the RPSEA program

Temperature testing verified the sensor can operate down to the freezing temperatures that could be experienced in ultra-deep water environments. In addition, the thermal cycling tests from 60°C to -1°C showed no fundamental weakness in the sensor. In the future thermal cycling tests will be conducted down to -20°C. The shock and vibration tests performed revealed no fundamental resonance conditions for the sensor. This demonstrates the sensor has a fundamentally solid design. A few points of physical rubbing were observed inside the sensor that caused small chips of the aluminum housing to be scraped off. The sensor has been modified to address this issue.

Testing of the transit case revealed the current packaging is not adequate for commercial shipping. The transit case will be upgraded in the next phase to ensure safe transit with commercial carriers.

The 13 month Phase 1 program was completed on schedule and RPSEA costs were slightly under budget.

The program will continue with Phase 2 in 2012 and 2013. Future developments include:

- 1) Upgrade window for 3000m depth operation
- 2) Open water trials of static imaging
- 3) Enhanced receiver and smaller packaging
- 4) Further development for survey capability
- 5) Further development of CONOPS and data deliverables for operators
- 6) Development for moving platform operation
- 7) Open water trials for moving platforms

The Phase 1 goals for this technology development program were all met and are still in-line with industry requirements. With the successes demonstrated in Phase 1, we envision that by the

end of Phase 2 the technology will be ready for demonstrations in ultra-deep water field operations to enable better integrity management of assets by providing real-time survey quality 3D data.

8 References

- ¹ J. Green, S. Matthews, and T. Turanli, "Underwater archaeological surveying using PhotoModeler, VirtualMapper: different applications for different problems," *International Journal of Nautical Archaeology*, vol 31, no. 2, pp. 283-292, 2002.
- ² P. Drap, J. Seinturier, D. Scaradozzi, P. Gambogi, L. Longd, and F. Gauche, "Photogrammetry for virtual exploration of underwater archeological sites," in *XXI International Scientific Committee for Documentation of Cultural Heritage (CIPA) Symposium*, Athens, Greece, October 2007.
- ³ G. Inglis and C. Roman, "Terrain constrained stereo correspondence," in *MTS/IEEE Oceans*, Biloxi, Mississippi, 2009.
- ⁴ C. Roman, G. Inglis, and J. Rutter, "Application of structured light imaging for high resolution mapping of underwater archaeological sites," *IEEE Oceans*, Sydney, Australia, 2010.
- ⁵ F. M. Caimi and D. M. Kocak, "Real-time 3D underwater imaging and mapping using a laser line scan technique," *Proc. SPIE Opt. Scan. Syst.: Design Appl.*, **3131**, 241-252, 1997.
- ⁶ F. M. Caimi and D. C. Smith, "Three-dimensional mapping systems and methods," U.S. Patent No 5,418,608, 1995.
- ⁷ S. Tetlow and J. Spours, "Three-dimensional measurement of underwater work sites using structured laser light", *Measurement Science and Technology*, vol. 10, no. 12, p. 1162, 1999.
- ⁸ E. Fuchs, "Multidimensional laser scanning system to test new concepts in underwater imaging", in *MTS/IEEE Techno-Oceans*, Vol.3, pp.1224-1228, 2004.
- ⁹ K. D. Moore, J. S. Jaffe, and B. L. Ochoa, "Development of a New Underwater Bathymetric Laser Imaging System: L-Bath," *Journal of Atmospheric and Oceanic Technology*, **17**, 1106 – 1115, 2000.
- ¹⁰ C. C. Wang and D. Tang, "Seafloor Roughness Measured by a Laser Line Scanner and a Conductivity Probe," *IEEE Journal of Oceanic Engineering*, Vol. 34, No 4, 459 – 465, Oct. 2009.
- ¹¹ J. W. McLean, "High Resolution 3-D Underwater Imaging", *SPIE Conference on Airborne and In-Water Underwater Imaging*, Vol. 3716, 10-19, 1999.
- ¹² Ulich et al., "Imaging Lidar System", U.S. Patent No 4,964,721, 1990.
- ¹³ M. Acharekar, "Underwater Laser Imaging System (ULIS)", *SPIE Vol. 3079*, 750-761, 1997.
- ¹⁴ J. McHale, "Navy moves to Ladar for Minehunting," *Military & Aerospace Electronics*, P.1, Vol.8, No.2, 1997.
- ¹⁵ N.G. Jerlov, *Marine Optics*, Elsevier, Amsterdam, 1976, pp. 231.
- ¹⁶ Baldrige, A. M., S.J. Hook, C.I. Grove and G. Rivera, 2009. The ASTER Spectral Library Version 2.0. Remote Sensing of Environment, vol 113, pp. 711-715. <http://speclib.jpl.nasa.gov>